

AD-A199 471

UDR-TR-88-89

(2)

DTIC FILE COPY

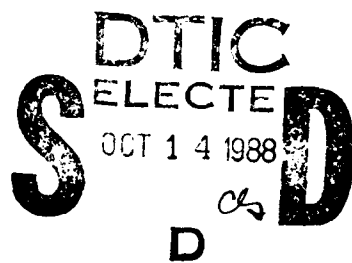
Evaluation of Optical Materials Samples

FINAL REPORT

Prime Contract No. DASG60-87-C-0029
Subcontract No. 8706 Modification A

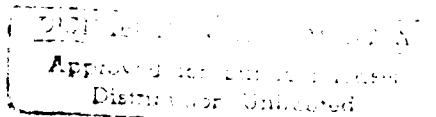
Prepared for:

Patel Engineers



Prepared by:

University of Dayton
Research Institute
Dayton, Ohio 45469



JULY 1988

88 9 26 062

TABLE OF CONTENTS

	PAGE
OBJECTIVE	1
WORK SCOPE	1
<u>Materials Characterization of Polycrystalline Si and SiC</u>	1
<u>AGT Damage Analysis - Electron and Ion Beam Effects</u>	2
<u>Cooled Mirror Corrosion Investigation</u>	2
RESULTS AND DISCUSSION	2
<u>Materials Characterization of Polycrystalline Si and SiC</u>	2
<u>AGT Damage Analysis - Electron and Ion Beam Effects</u>	4
<u>Cooled Mirror Corrosion Investigation</u>	28
APPENDIX A	53



per ltr.

A-1

LIST OF FIGURES

	PAGE
1 View of cooled mirror showing exposed face-plate support posts.	3
2 Close-up view of support posts and coolant channels.	3
3 Electron beam damage at crater #1. A 10 KeV electron beam at 2 microamps was rastered over a 125 micron by 88 micron region.	6
4 Electron beam damage at a site well away from any apparent pit damage.	6
5 Damage blisters which resulted from 12.5 minutes ion beam sputtering at 2 KeV.	8
6 Sputter crater after 16 minutes of sputtering.	8
7 An Auger spectrum from inside crater #2 just below the central pit.	9
8 Crater #2 after the ZnSe layer had been sputtered away.	11
9 An Auger spectrum from the far left portion of Figure 8 along the line scan.	12
10 An Auger spectrum from the left rim of crater #2 along the line scan.	13
11 An Auger spectrum from within the perimeter of crater #2 just below the central pit.	14
12 An Auger spectrum of ThF_4 immediately after the ion beam was turned off.	16
13 An Auger spectrum of ThF_4 immediately after the ion beam was turned off.	17
14 A secondary electron image of crater #2 at the silver/chromium/silicon interface.	18
15 An Auger spectrum from within the crater rim just below the central pit.	19
16 An Auger spectrum taken from a region above the damage site.	21
17 Silicon substrate at the crater #2 site.	22

18	Compositional backscatter electron image of crater #2 after sputtering.	22
19	A topographical backscatter electron image of crater #2 after sputter.	23
20	Crater #3 with the optical overlayers sputtered away.	25
21	An Auger spectrum of the central feature in Figure 20.	26
22	Topographical backscatter image of crater #3 after sputtering.	27
23	White crystalline-like "corrosion" material found in the area of the face-plate support posts (25X).	29
24	SEM photomicrograph of porous SiC with "corrosion" material filling the pores.	29
25	EDAX scan of porous SiC and contaminant showing the presence of Mn, Ca, Si, and Al.	30
26	EDAX scan of porous SiC and contaminant showing the presence of Al, Si, K, Ca, Mg, and Fe.	30
27	Laser mirror mount contaminated region 1.	33
28	SiC piece next to region with pin broken off AES scan.	36
29	SiC and B ₄ C AES surface scan.	42
30	SEM photomicrograph of fracture porous SiC (region 1) and contaminant (region 2) as observed by ACS.	45
31	SEM photomicrograph of region 1.	45
32	SEM photomicrograph of region 2.	46
33	Porous SiC (side w/pins broken off) ESCA surface scan.	47

LIST OF TABLES

	PAGE
1 XRD RESULTS - POROUS SiC	10
2 COOLED MIRROR POROUS SiC SURFACE	32

Characterization Studies for Advanced Mirror Materials

OBJECTIVE

The primary objective of order subcontract was to prepare AGT and UGT test specimens, provide characterization data and provide damage assessments on tech base laser mirror materials being developed on other government contracts. The properties to be determined included flexural strength, Young's modulus, Poisson's ratio, fracture toughness (K_{Ic}), coefficient of thermal expansion, thermal diffusivity, hardness, and specific heat. In some cases scanning electron microscopy (SEM), x-ray diffraction (XRD), energy dispersive x-ray analysis (EDAX), and Auger spectroscopy (AES) were to be performed to determine chemical composition and crystal structure and damage mechanisms. In addition if materials problems occurred, that could not be anticipated in advance, studies were to be initiated to aid the SDI optical materials efforts as required.

WORK SCOPE

Materials Characterization of Polycrystalline Si and SiC

The majority of the materials characterization work accomplished in this program was performed on materials prepared by chemical vapor deposition (CVD). The CVD prepared materials were supplied by two companies, Raytheon Corporation and CVD Incorporated, who were funded by the New Materials Division of the Rapid Optical Fabrication Technology (ROFT) program. Both of the firms supplied polycrystalline silicon (Si) and silicon carbide (SiC) test specimens or bulk material for test specimens preparation. Two additional commercial materials were supplied by Dr. Alan Hopkins, AFWL/AR-2, Kirtland AFB, New Mexico. The two materials were labeled SA and ST. No additional information was provided.

AGT Damage Analysis - Electron and Ion Beam Effects

Specimens obtained from the Naval Weapons Center (NWC) were analyzed using the Scanning Auger Spectrometer at UDRI. The purpose of the investigation was to determine the damage mechanisms associated with ZnSe/ThF₄/Ag/Cr coatings on single crystal silicon substrates after exposure to high energy electron and ion beam sources.

Cooled Mirror Corrosion Investigation

A significant portion of the effort in this program resulted from an unexpected problem that developed with a cooled mirror system under development at United Technologies Optical Systems. What appeared to be a severe corrosive type chemical reaction occurred in a portion of the heat exchanger (Figure 1) after a successful water pressure test had been performed on the heat exchanger. At first, impurities in the cooling water used in the pressure test, or cooling water used to machine the porous SiC isolation plate (Figure 2), were suspected to contain elements that reacted with SiC exchanger materials. Also, an organic wax material used in the machining process was suspected as a possible contributor to the problem. However, preliminary results obtained at UTOS using SEM, EDAX, and fourier transform infra-red spectroscopy (FTIR) to analyze the white, powder-like "corrosion product" did not confirm this assumption. Consequently, the heat exchanger assembly was sent to UDRI for examination.

RESULTS AND DISCUSSION

Materials Characterization of Polycrystalline Si and SiC

The materials characterized include single crystal silicon (Si), CVD prepared polycrystalline Si, CVD prepared polycrystalline silicon carbide (SiC), and reaction bonded, commercially available, SiC.

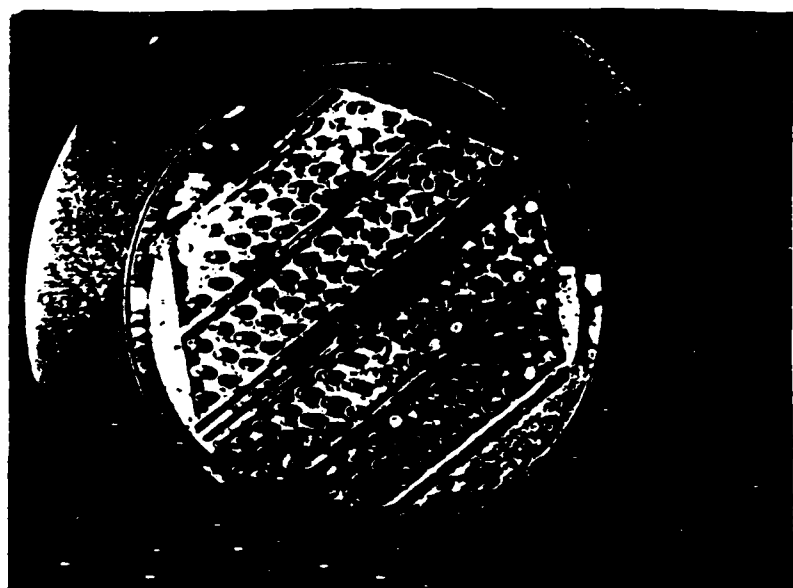


Figure 1. View of cooled mirror showing exposed faceplate support posts.

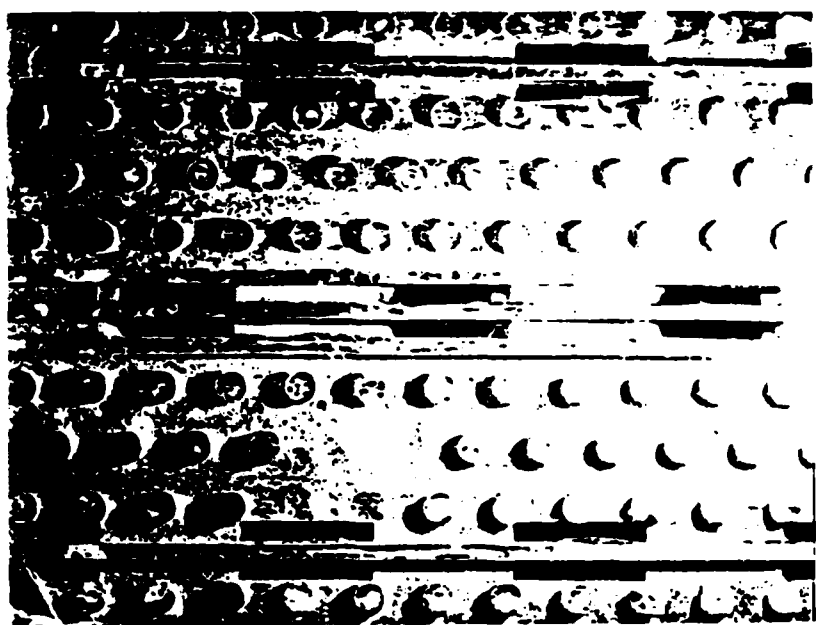


Figure 2. Close-up view of support posts and coolant channels.

Appendix A is a compendium of mechanical and thermal property data obtained from the silicon (Si) and silicon carbide (SiC) materials. These materials were tested at UDRI large optics and cooled mirror programs in support of mirror materials development programs sponsored by with U.S. Air Force and SDIO.

The wide variety of materials tested and the brittle nature of Si and SiC precludes a concise listing of materials properties, especially mechanical. We have, therefore, listed each group of test specimens separately and have included comments specific to each material. These include what is known about material fabrication processes, pre-test surface treatment or condition, crystallographic orientation (if single crystal) or preferred orientation (if polycrystalline), post-test fracture analysis observations, microstructure (if observed), and the number of specimens included in the analysis.

Designers of structural components using these materials should keep in mind that the mechanical properties of these materials are greatly affected by crystallographic orientation, surface finish and/or treatment, sub-surface damage, microstructure, etc. This data should be used only as a guide in design considerations and provisions should be made to obtain witness specimens from the material stock intended for construction of a device. These specimens should then be prepared and tested using conditions as near as possible to those expected in actual use.

AGT Damage Analysis - Electron and Ion Beam Effects

Specimen 6-3788-2 supplied by II-VI Inc. was examined using scanning Auger spectroscopy. The coating design is described as ZnSe/ThF₄/Ag/Cr on a silicon substrate and having a gold over-layer as a result of previous SEM analysis before delivery to the University of Dayton.

A sacrificial crater was selected to enable Auger instrumental parameters to be adjusted. After nearly one hour of rastering the electron beam over an area of interest, severe damage was noted as shown in Figure 3. Auger spectroscopy requires a sufficient focused electron beam with enough current to initiate a sufficient number of Auger events to enable detection. Beam currents on the order of 0.1 microamps or greater are usually required. This is well above what is ordinarily required for SEM/EDS analysis. It is not uncommon, therefore, to detect beam damage in radiation sensitive specimens. If a damage threshold can be determined, successful Auger analysis is accomplished by choosing parameters well below the critical current density. The current density can be greatly reduced by rastering the electron beam over a broad area compared to the actual beam diameter. The degree of damage observed in the rastered area shown in Figure 3 was totally unexpected. Our previous experience with ZnSe indicated that specimen charging could be a major problem but none was observed. The "melting", cracking, and blistering observed in Figure 3 were not observed in previous ZnSe studies.

To eliminate the possibility that the observed damage was somehow related to localized pit damage, another region well away from any damage craters was selected. A 10 KeV beam at 2 microamps was rastered over a 77 x 56 micron rectangle for approximately 1 hour. The results are shown in Figure 4. Cracking, blistering, and melting are again observed. Some blistering damage is apparent even outside the rastered area. The power density under these conditions was calculated to be on the order of 500 watts/cm² which is relatively low. The damage appears to be confined to the ZnSe layer:

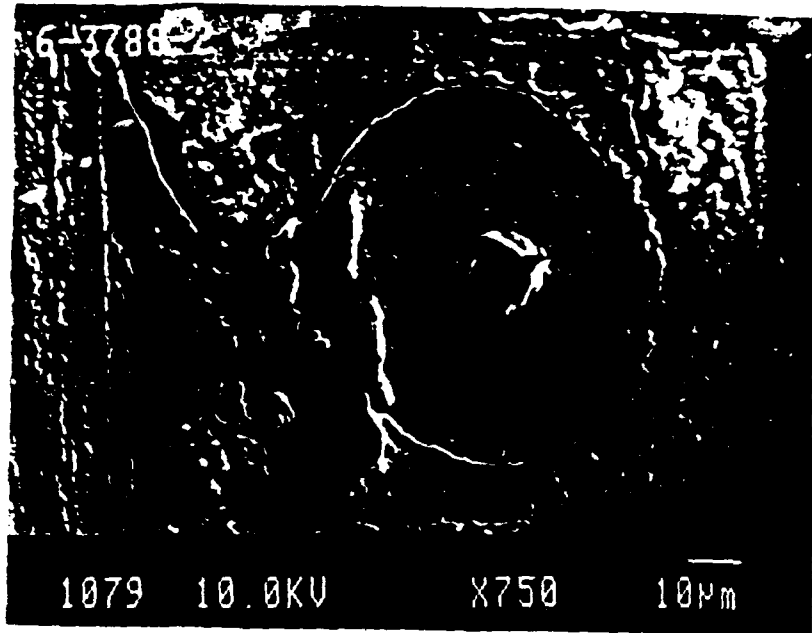


Figure 3. Electron beam damage at crater #1. A 10 KeV electron beam at 2 microamps was rastered over a 125 micron by 88 micron region. Melting, blistering, and cracking damage is apparent.

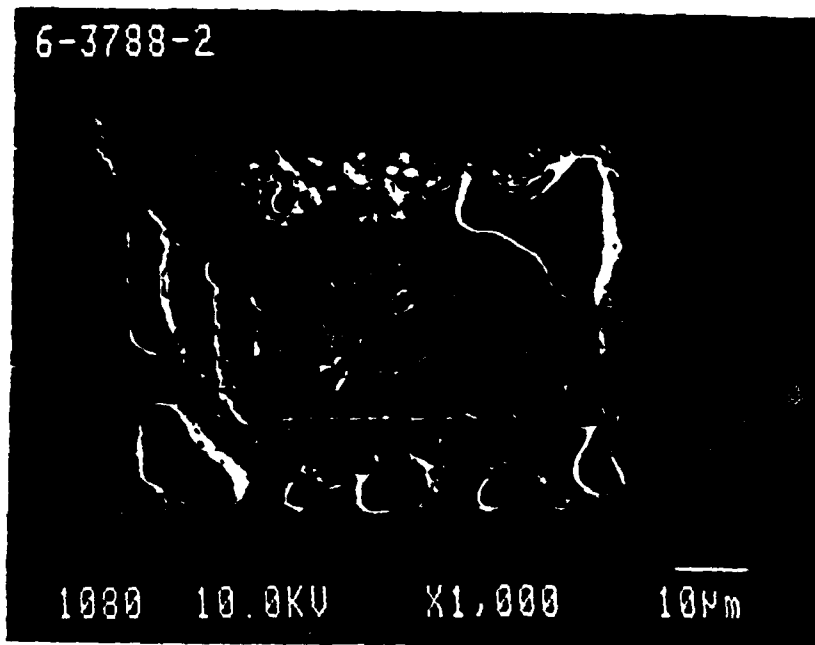


Figure 4. Electron beam damage at a site well away from any apparent pit damage. Damage is apparent within the confines of the rastered region as well as outside the region suggesting that this specimen is a poor heat conductor.

A focused argon ion beam was used to determine whether any localized damage would result from sputtering the ZnSe layer. Again, a region well away from any damage craters was selected. Figure 5 shows what appears to be small blisters on the order of a few microns in diameter after about 12.5 minutes of sputtering at a current density of approximately 1.5×10^{-4} amps/cm², which is two orders of magnitude lower than calculated for the electron beam current density in Figure 4 which was 4.6×10^{-2} amps/cm². Figure 6 shows the sputter crater after 16 minutes of sputtering. The central region of this crater resulted from both ion and electron beam damage. In a typical ion beam sputter crater one would anticipate seeing a shallow generally featureless crater. These results again suggest this specimen is a very poor conductor of heat. Whether this damage results from previous damage inflicted by laser irradiation or is characteristic of this particular ZnSe coating is not known. The major point of concern is that such catastrophic damage can be induced at relatively low power levels of e-beam and ion beam irradiation. Additional sputtering revealed that the sputtering effects seen in Figure 6 vanished as the ZnSe layer was penetrated. The ThF₄ underlayer appeared flat and features within the ion beam perimeter.

• Auger Analysis

Once it was established that the ZnSe layer was subject to electron and ion beam damage with no apparent acceptable damage threshold for Auger analysis, parameters were chosen which minimized the beam effects in the ZnSe film. A damage crater designated crater #2 was chosen. Figure 7 is an Auger spectrum taken from within this crater. Sulfur, carbon, silver, oxygen, fluoride, zinc, selenium, and silicon are observed. Sulfur, carbon, and oxygen are most likely from ordinary environmental contamination as a

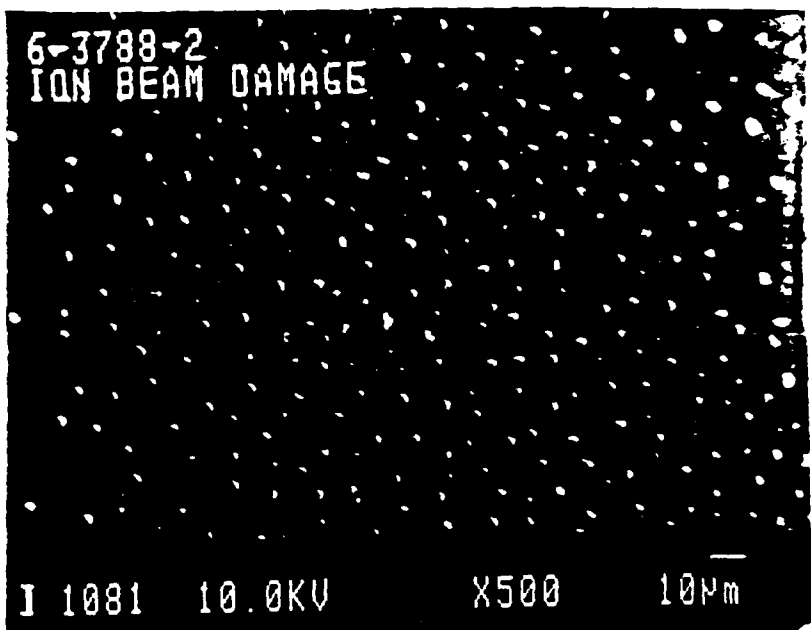


Figure 5. Damage blisters which resulted from 12.5 minutes ion beam sputtering at 2 KeV. The ion beam current density was at least 2 orders of magnitude lower than the electron beam current density used in Figure 2.

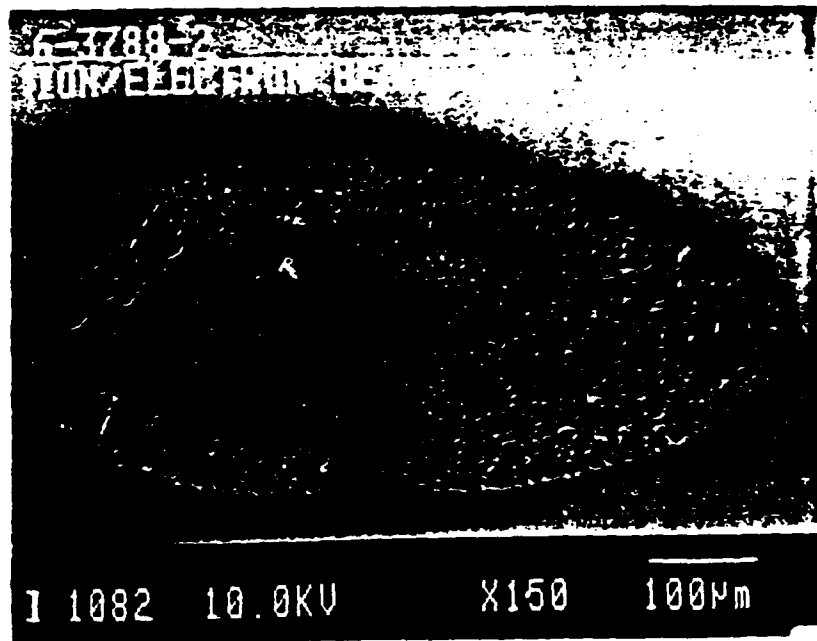


Figure 6. Sputter crater after 16 minutes of sputtering. The damage at the center of the crater resulted from both electron and ion beam damage.

6-3788-2, DAMAGE DEBRIS WITHIN CRATER #2

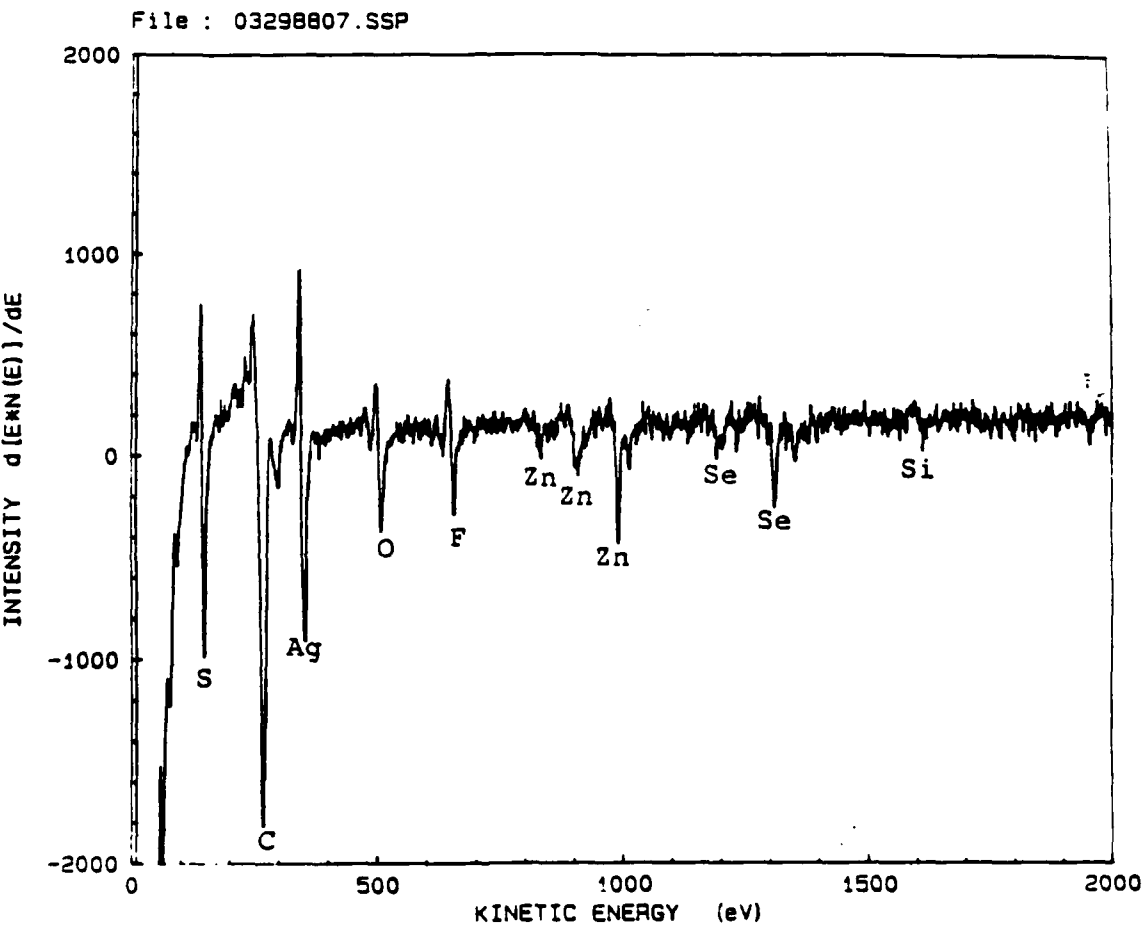


Figure 7. An Auger spectrum from inside crater #2 just below the central pit. The absence of thorium is significant.

result of handling. Zinc and selenium are from the outermost optical coating. The presence of silver and fluoride along with the absence of thorium is curious.

Crater #2 was ion sputtered for a sufficient period of time to remove the surrounding ZnSe layer. Figure 8 shows crater #2 with the ZnSe layer etched away. Auger line scan for silver is superimposed on this photograph along with the actual line which was scanned. It is evident that a ring containing a significant amount of silver forms the crater rim. Larger concentrations of silver are apparent within the crater than immediately outside. There is a halo region surrounding the crater edge about 10 microns wide where the silver level reaches a minimum. Beyond this the silver concentration again increases. We suggest that this could result from debris expelled from the crater during catastrophic failure. It is almost certainly not an ion beam effect. Auger spectra were acquired in regions (from Figure 8) to the left of the halo (Figure 9), on the rim of the crater (Figure 10), and in the crater below the center pit (Figure 11). Table 1 shows the elemental concentrations from these three regions in atomic percents.

TABLE I
XRD RESULTS - POROUS SiC

Region	Thorium	Silver	Oxygen	Fluoride
Left of Crater	45.3	2.7	46.3	5.7
Crater Rim	41.3	5.6	44.1	8.9
In Crater	43.4	2.4	48.7	5.5

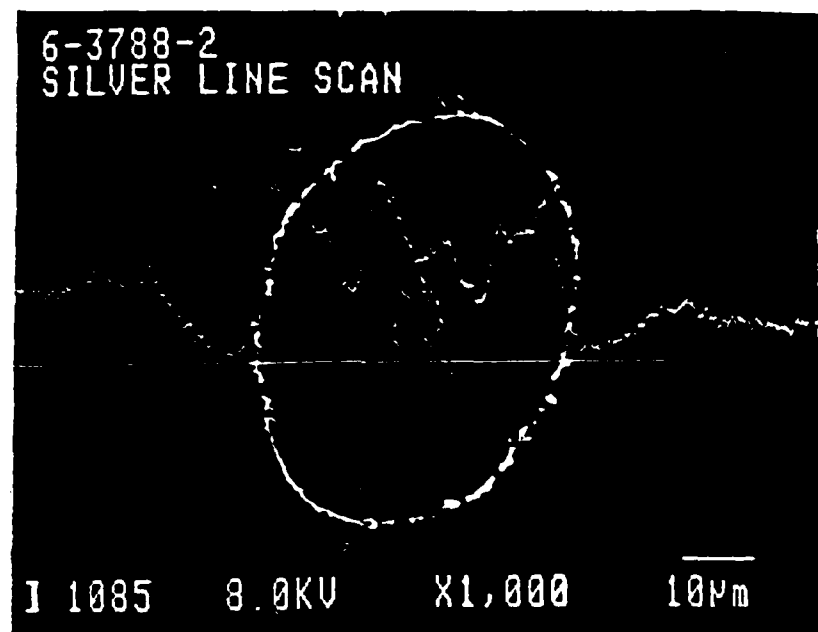


Figure 8. Crater #2 after the ZnSe layer had been sputtered away. A silver Auger line scan is superimposed along with the actual line which was scanned. Silver is present in all but the 10 micron halo region immediately adjoining the crater rim.

6-3788-2. FAR LEFT REGION OF LINE SCAN

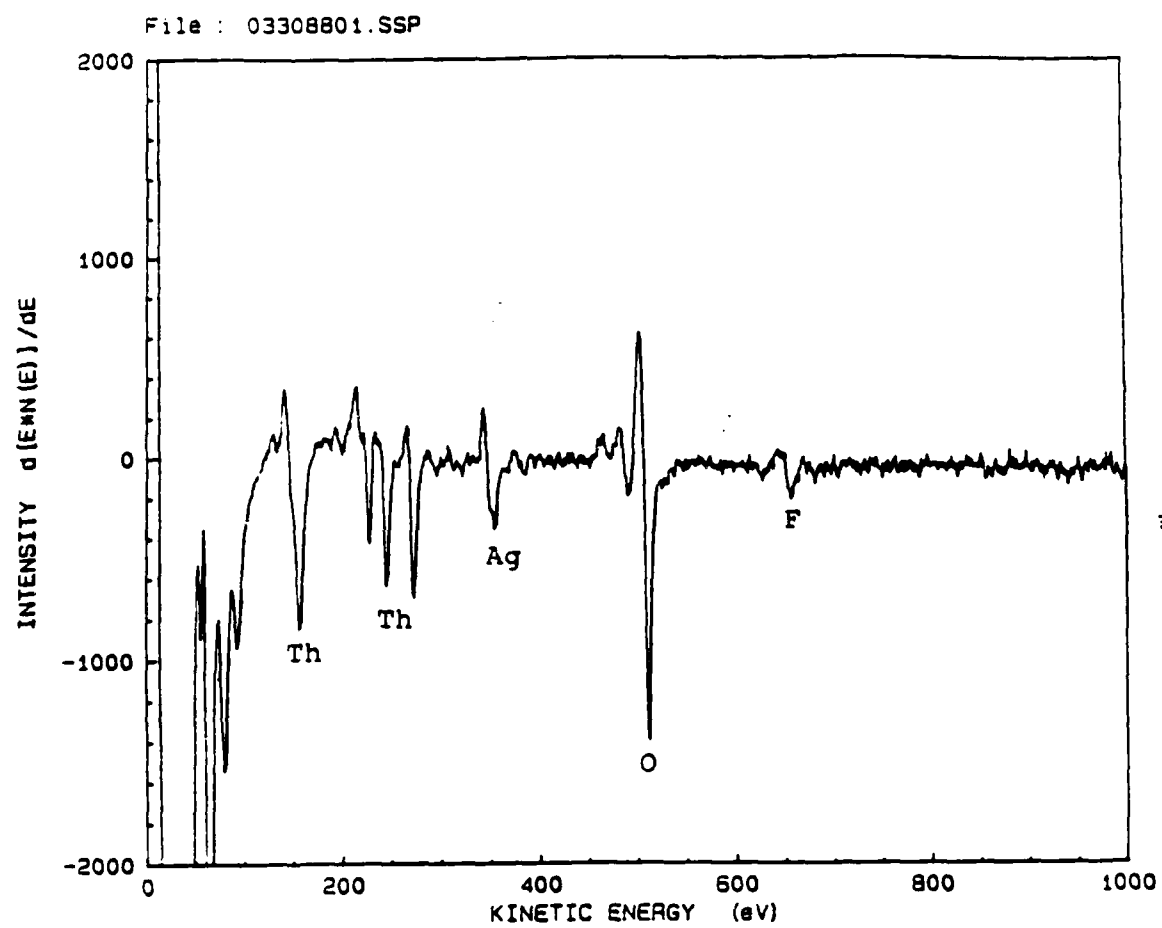


Figure 9. An Auger spectrum from the far left portion of Figure 8 along the line scan.

6-3788-2. LINE SCAN, LEFT RIM OF CRATER

File : 03308802.SSP

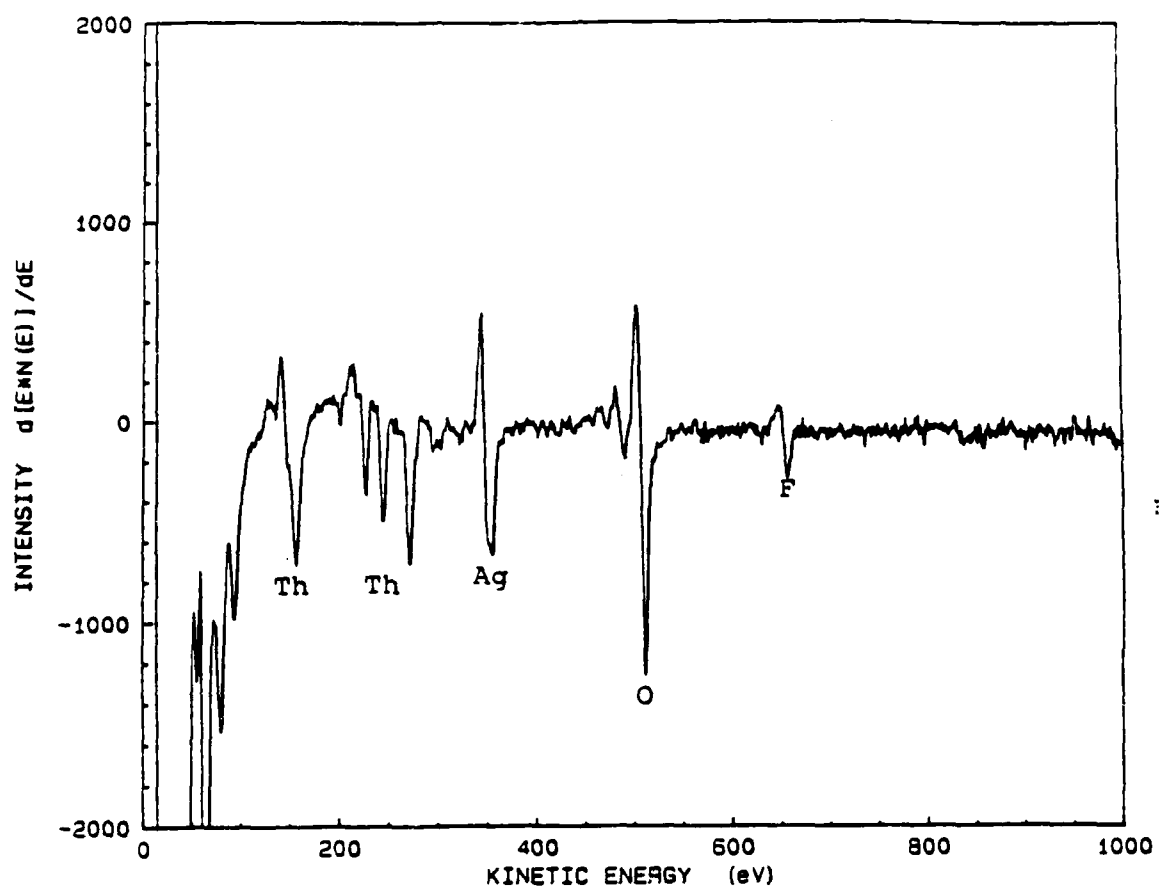


Figure 10. An Auger spectrum from the left rim of crater #2 along the line scan.

6-3788-2. WITHIN CRATER, BELOW CENTER OF LINE SCAN

File : 03308803.SSP

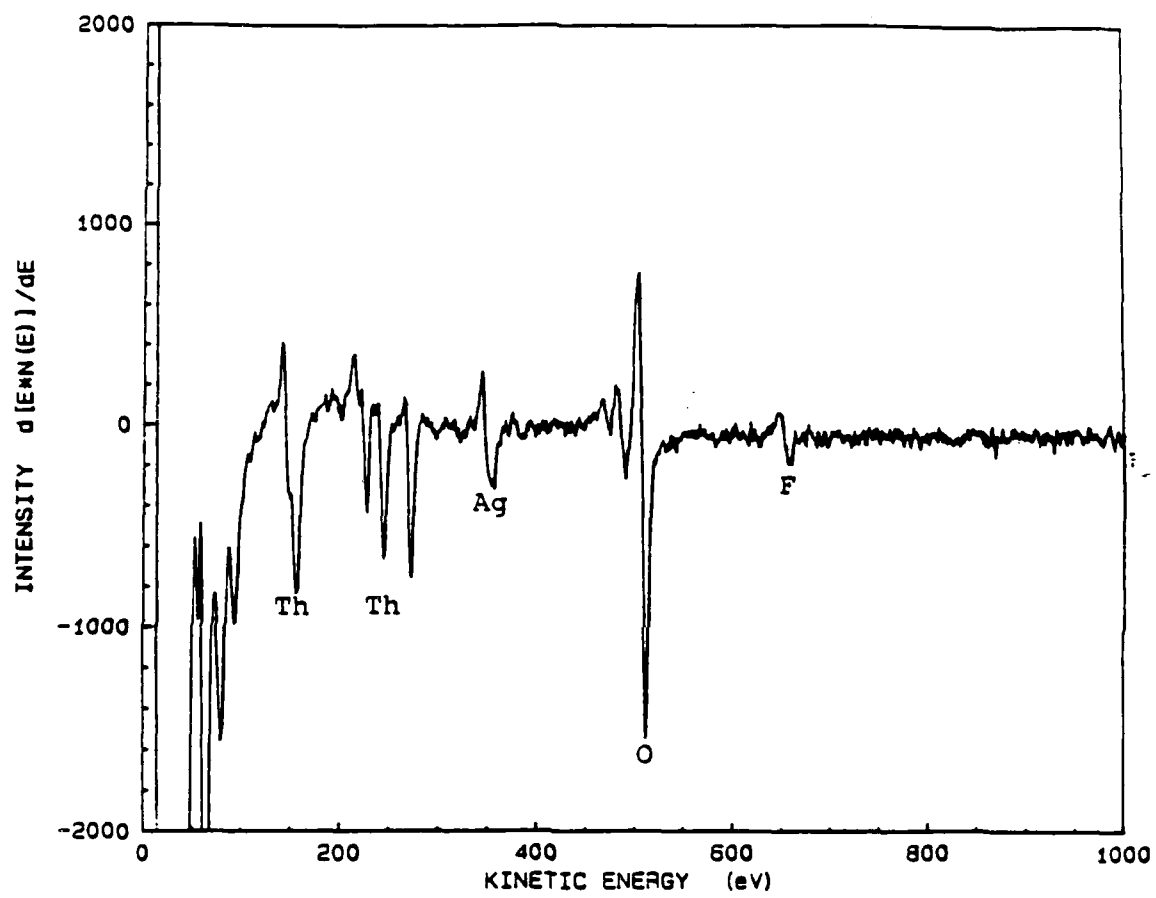


Figure 11. An Auger spectrum from within the perimeter of crater #2 just below the central pit.

Thorium fluoride presents several problems with regard to Auger spectroscopy. It is known from the literature and from our previous experience with calcium fluoride, that electron beam desorption of fluorine will almost certainly occur during Auger analysis. Consequently the levels measured with Auger spectroscopy may not reflect actual fluoride (fluorine) concentrations in an unperturbed specimen unless damage thresholds are established. Further, with ThF_4 , as fluoride is desorbed, the vacated sites are highly energetic and will tenaciously getter oxygen, even at pressures in the 10^{-7} Pa range. The fluorine and oxide concentrations shown in Table 1 must be interpreted in terms of these e-beam phenomena. Further, these anomalies can be shown graphically just by turning off the ion beam and comparing Auger spectra. Figure 12 is an Auger spectrum from the ThF_4 layer with the argon ion beam on. Figure 13 is an Auger spectrum taken from the same region immediately after the ion beam was turned off. The pressure at the specimen during this analysis was in the low 10^{-6} Pa range. The desorption of fluorine could be demonstrated by watching the fluorine peak decrease as a function of electron beam irradiation time.

We conclude from Table 1 that the oxygen level is artificially high and probably results from exposure to oxygen during catastrophic failure as well as from oxygen gettered from the Auger vacuum system. The fluoride level is most definitely reduced by the Auger analysis and may also be further reduced during catastrophic failure if temperatures reach excessive levels. It is interesting to note that the fluoride level increases as the silver fluoride compound may be a reaction product in this failure mode. This could also explain the presence of fluoride in Figure 7 where thorium is not detected.

Figure 14 shows crater #2 at the silver/chromium/silicon interface. Figure 15 is an Auger spectrum taken inside the crater rim. Silver,

6-3788-02. THORIUM FLUORIDE WHILE SPUTTERING

File : 03298804.SSP

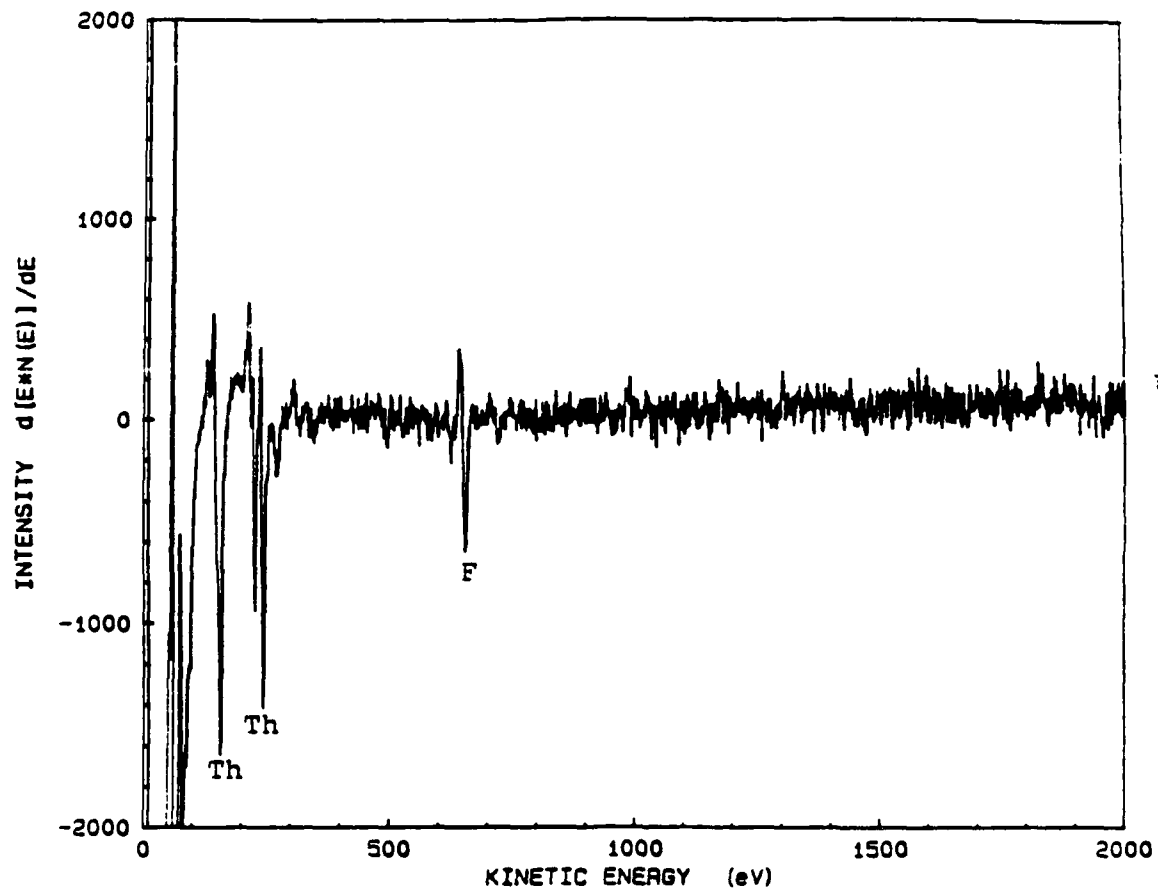


Figure 12. An Auger spectrum of ThF_4 immediately after the ion beam was turned off. Note the absence of oxygen which would occur near 510 eV.

6-3788-02. THORIUM FLUORIDE. ION GUN OFF

File : 03298802.SSP

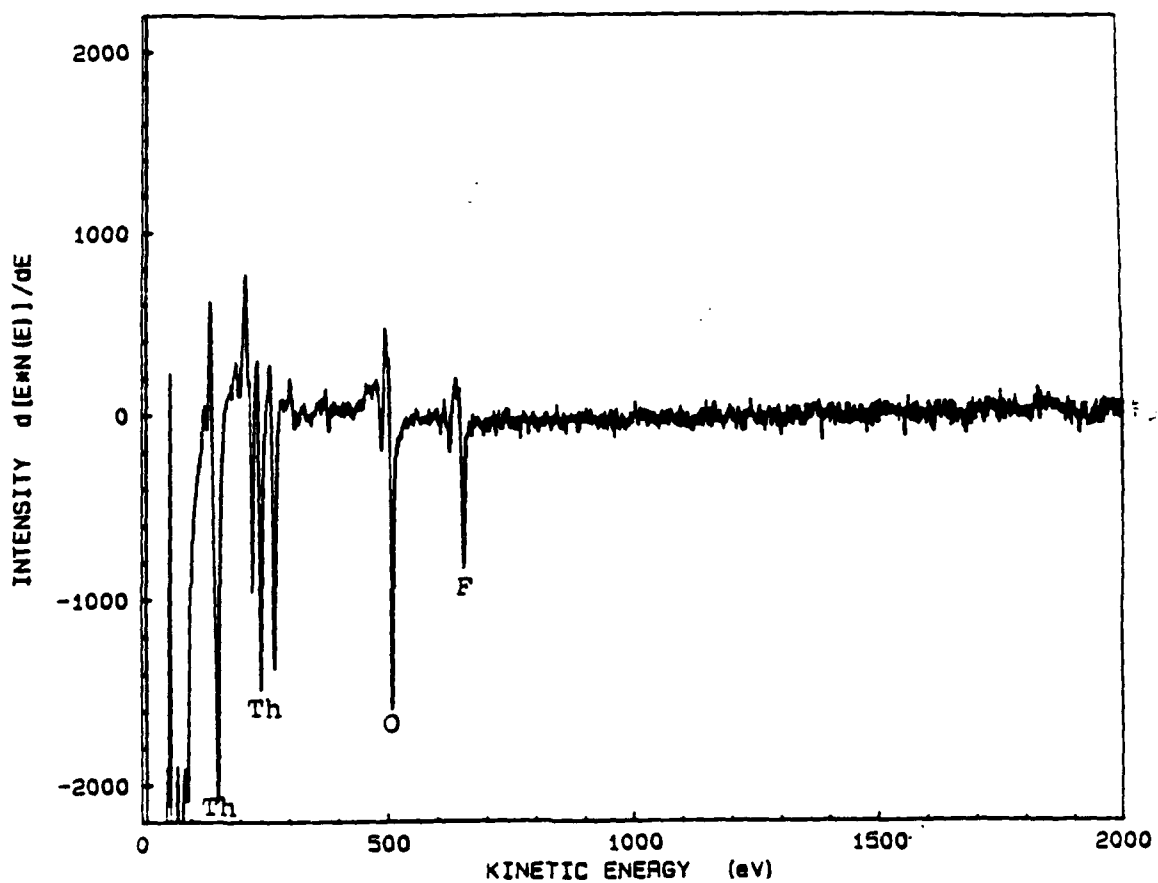


Figure 13. An Auger spectrum of ThF_4 immediately after the ion beam was turned off. Note the large oxygen peak at 510 eV.

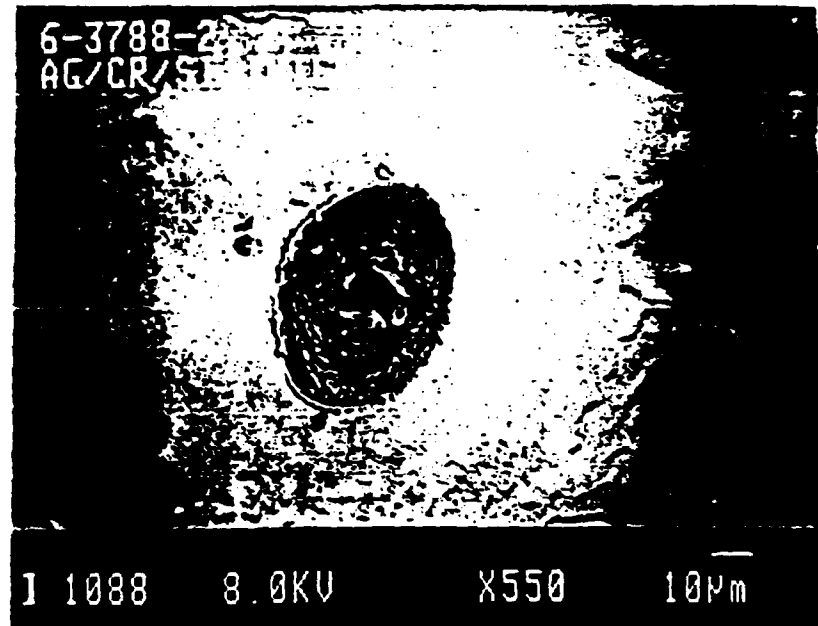


Figure 14. A secondary electron image of crater #2 at the silver/chromium/silicon interface. There appears to be some blistering at the silver/thorium fluoride interface along the right edge and at the bottom of this micrograph.

6-3788-2. AG/CR/SI INTERFACE IN CRATER #2

File : 03308804.SSP

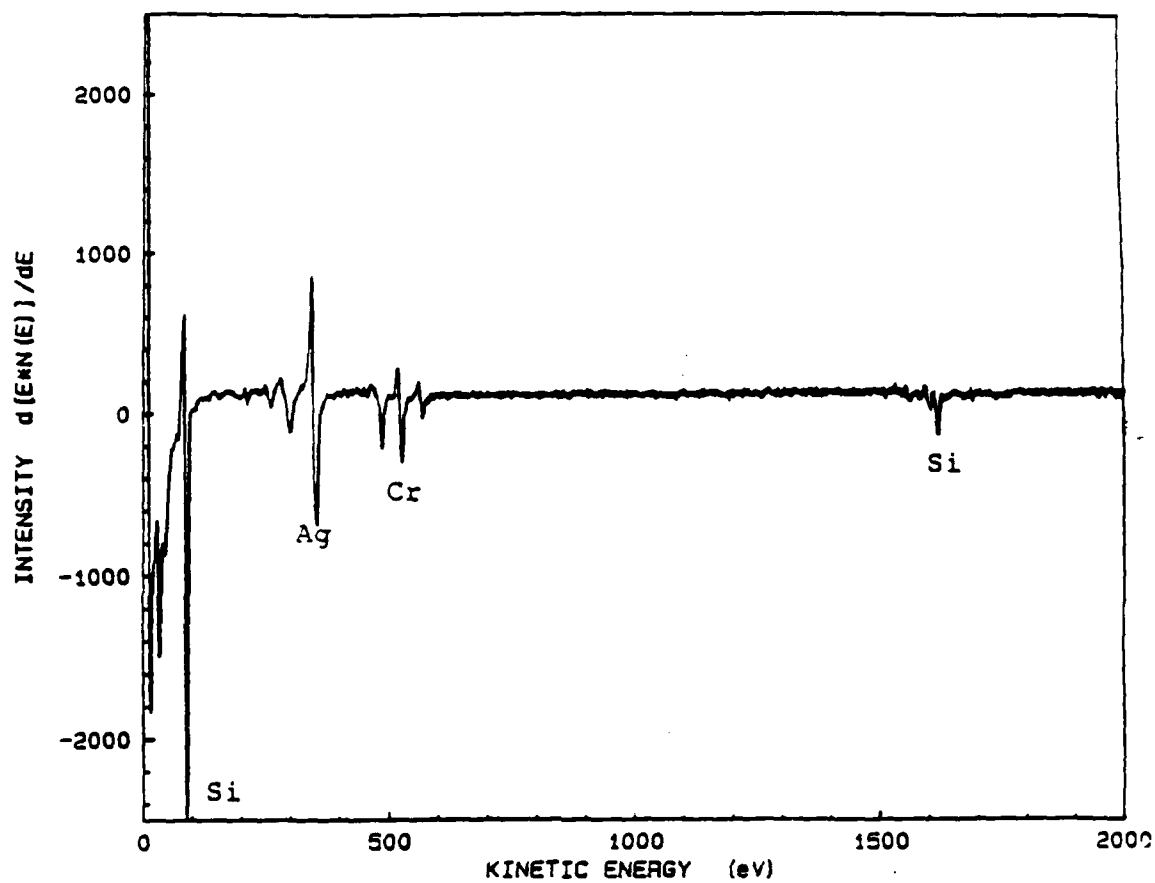


Figure 15. An Auger spectrum from within the crater rim just below the central pit. Silicon, chromium, and silver are present.

chromium, and silicon are present. The light colored region outside the crater is silver as shown by the Auger spectrum in Figure 16. It is interesting to note that silicon and chromium are seen within the crater and only silver is seen outside the crater even though both regions were sputtered for the same period of time. This suggests that most of the silver was expelled from the crater during failure. This is consistent with the Auger results. The gray region near the right and left hand edges of Figure 14 is the ThF_4 film. It appears that some blistering has occurred. Whether this is significant is unknown. This damage could very well be caused by the ion beam.

Figure 17 shows crater #2 with most of silver and chromium sputtered away. A feature in the center of this crater which could be a defect in the silicon is apparent. Further, roughness in the area within the crater rim suggests that the silicon substrate may have undergone localized melting during catastrophic failure.

A composition backscatter electron image from crater #2 is shown in Figure 18. Heavier elements with larger backscatter coefficients appear bright whereas lighter elements appear darker in color. Auger spectra confirm that the light areas are rich in silver and chromium whereas the gray region is pure silicon.

A topographical backscatter image of crater #2 is shown in Figure 19. The center defect, the silver rich crater rim, and the rough surface within the crater are clearly visible. The features at the upper left of the crater could be from expelled debris or possibly other subsurface defects. Defects in the silicon substrate such as a pits or subsurface voids could well serve as failure nucleation sites because of their inability to dissipate heat evenly. Cratering could then occur expelling debris from the

6-3788-2, SILVER FILM ABOVE CRATER #2

File : 03308805.SSP

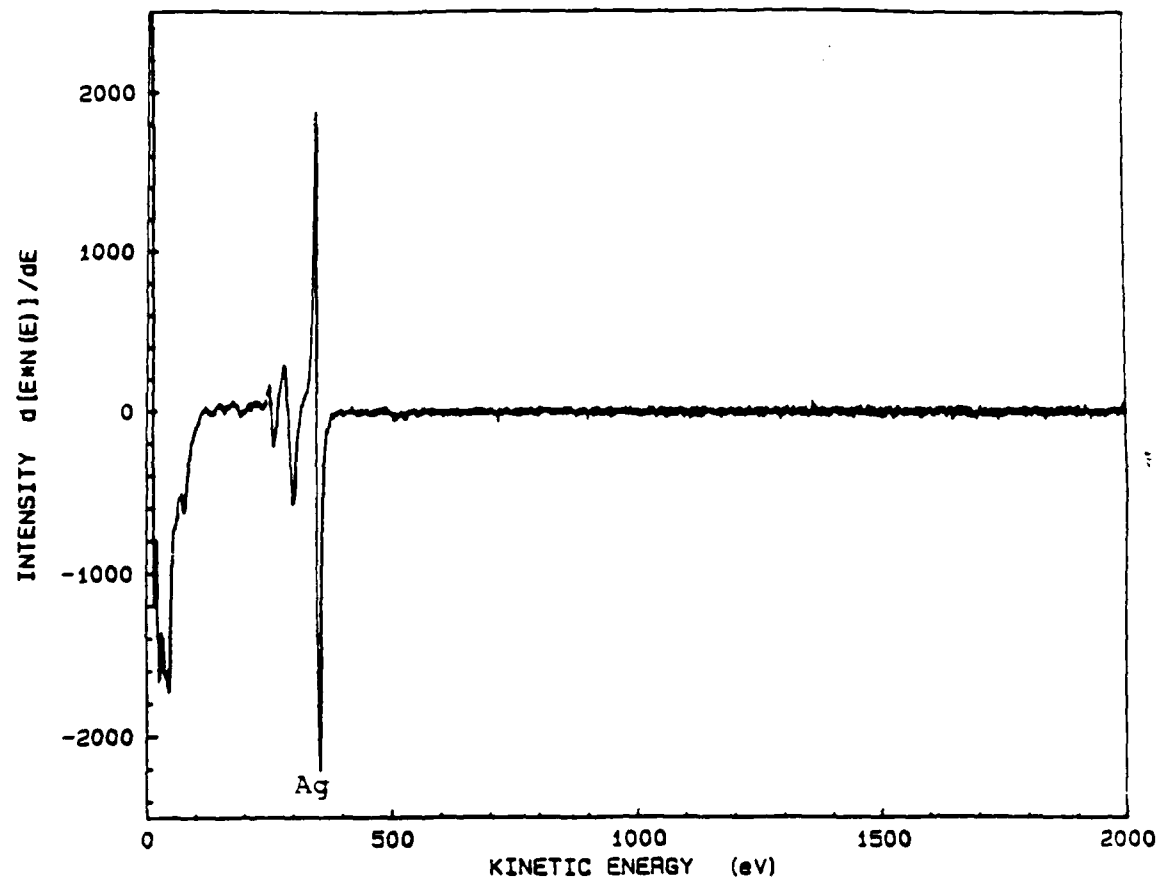


Figure 16. An Auger spectrum taken from a region above the damage site. Silver is the only element present.



Figure 17. Silicon substrate at the crater #2 site. A pit is observed at the center of this crater. If this defect was present before testing, it could have been responsible for the failure of this film at this site.

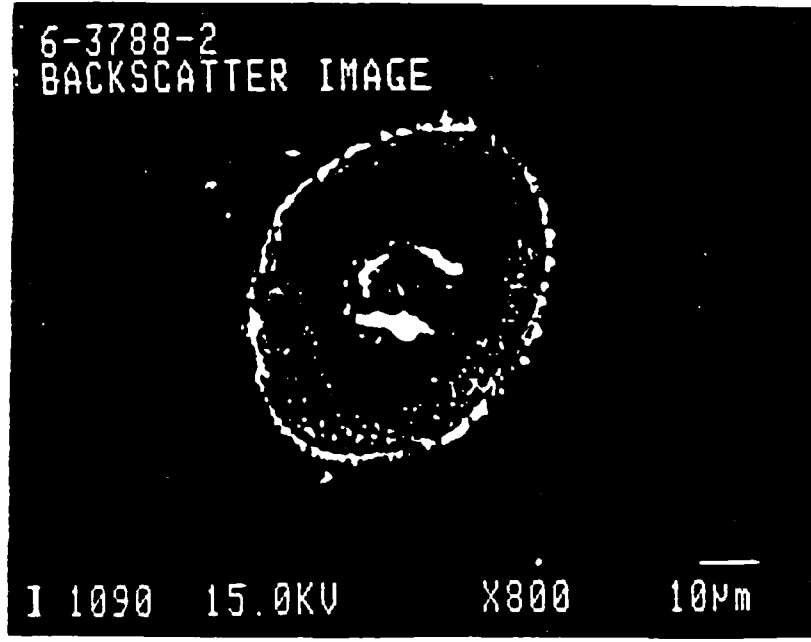


Figure 18. Compositional backscatter electron image of crater #2 after sputtering. The bright regions indicate the presence of heavy elements (silver and chromium) whereas the neutral gray region indicates the silicon substrates.

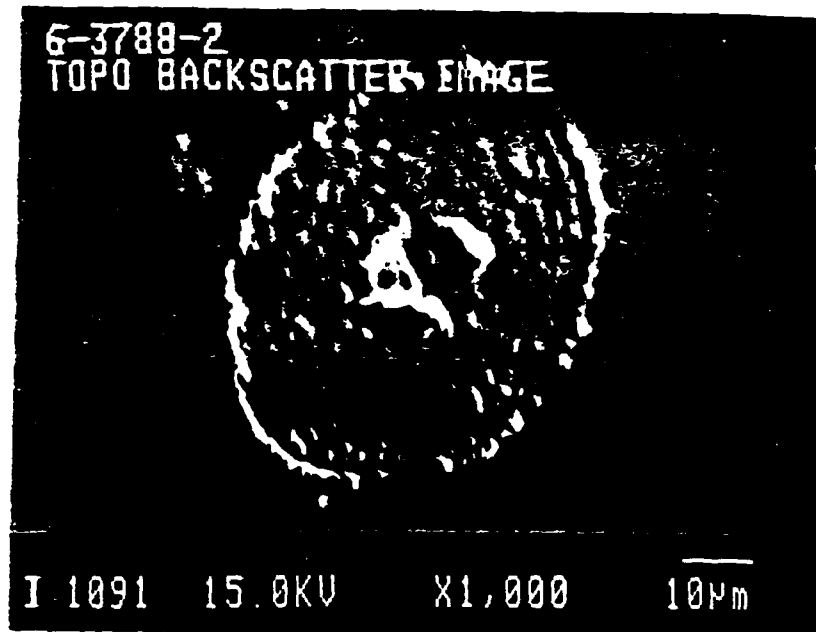


Figure 19. A topographical backscatter electron image of crater #2 after sputtering. This failure has changed the surface topography. It is not unreasonable to suspect that the failure originated at the central defect leading to subsequent localized melting of the silicon substrate and the optical coating overlayers.

inner most layers which would end up inverted within the crater debris near the rim. This cratering mode of failure would explain the presence of silver in the crater debris spectrum shown in Figure 7. Depending on temperatures during failure, localized melting of the silicon substrate could occur leaving an uneven surface after resolidification.

A second crater was sputtered (designated crater #3) to determine if a central defect in the silicon substrate could be detected. Figure 20 shows crater #3 with the ThF_4 and ZnSe layers sputtered away. Again, a silver rich crater rim is observed and a textured region within the rim clearly visible. A feature on the order of 1 micron in diameter is visible near the center of this crater. Figure 21 is an Auger spectrum from this central feature. Silver, chromium, and silicon are present and perhaps alloyed because of heat generated upon failure. Figure 22 is a topographical back-scatter electron image of crater #3. There is no evidence of a topographical defect at the center of this crater. It is quite possible, however, that if the substrate became hot enough to melt, any topographical submicron defect may have been smoothed over upon solidification. No evidence of aluminum oxide or any other polishing agent was found. This does not eliminate the possibility that embedded polishing agents could serve as failure sites. If residual polishing compounds caused the failure at crater #3, they may have been expelled with other crater debris or were present in amounts below the detectability limit of Auger spectroscopy. It is also possible that a subsurface void may have caused the damage seen in crater #3.

There is no clear evidence that the failures at craters 2 and 3 were caused by impurities in the optical films. We suggest that the crater

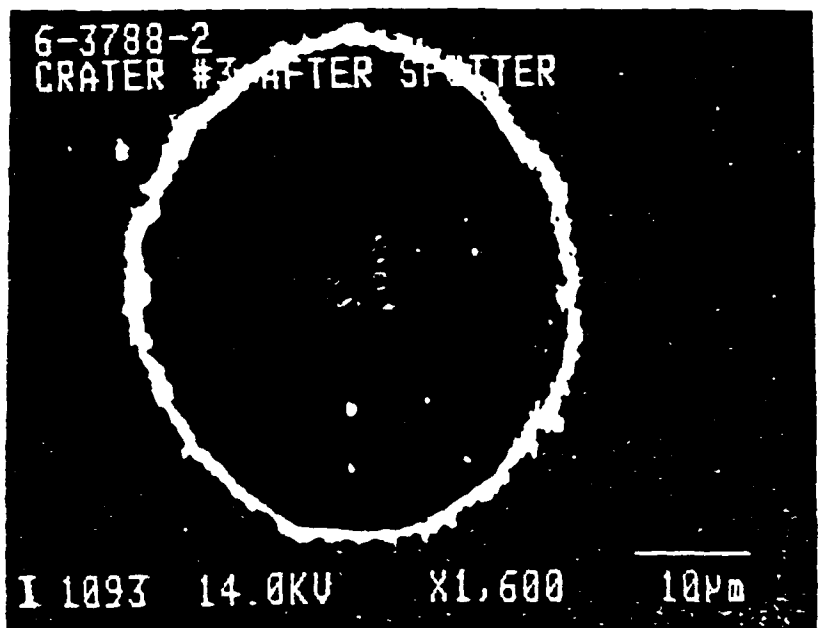


Figure 20. Crater #3 with the optical overlayers sputtered away. As with crater #2, a crater rim containing silver and chromium remains. There is evidence of a central defect. It also appears that melting and resolidification occurred within the confines of the crater rim.

6-3788-2. CENTER FEATURE IN CRATER #3

File : 03318806.SSP

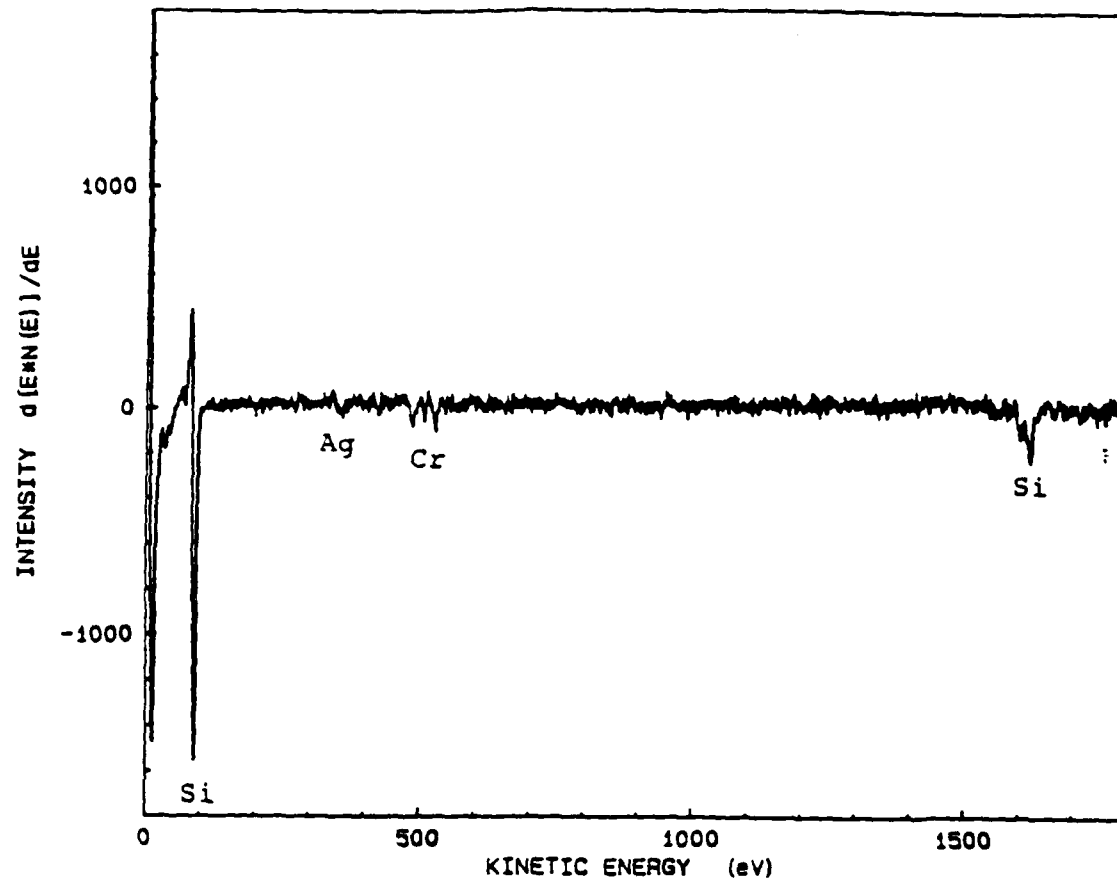


Figure 21. An Auger spectrum of the central feature in Figure 20. Silver, chromium, and silicon are present and perhaps have alloyed as a result of heat generated during failure.

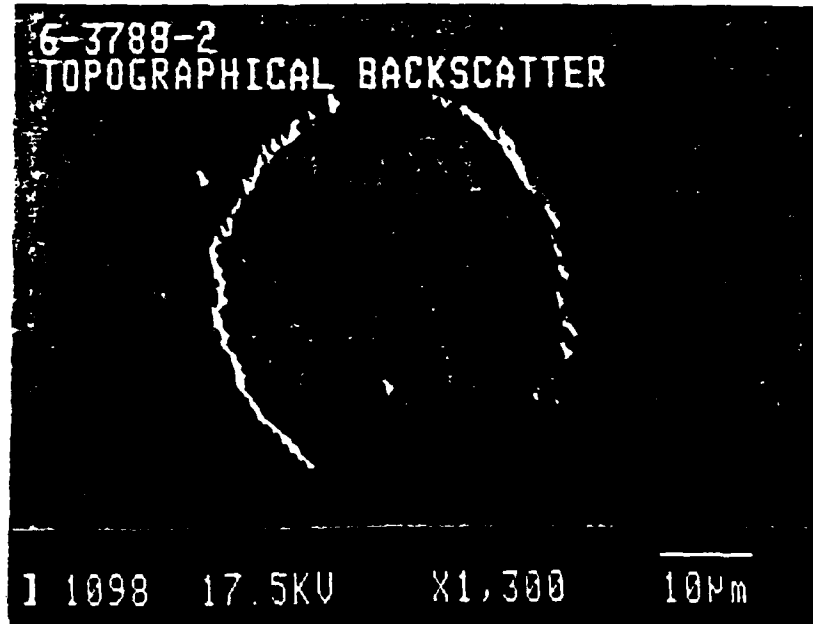


Figure 22. Topographical backscatter image of crater #3 after sputtering. The crater rim and the textured region within the crater are clearly visible.

failures observed on this specimen are related to substrate defects rather than film defects although this is conjecture on our part.

Cooled Mirror Corrosion Investigation

All of the work performed in this phase of the investigation was directed towards the investigation of the failure of a high energy laser (HEL) cooled mirror failure. Dr. Alan Hopkins delivered to UDRI a Universal Technology Optical Systems (UTOS) cooled mirror (Figure 1) that had developed cracks in an area directly under the faceplate where several water passage channels were located (Figure 2). The area affected by the fracture problem was made of an interconnecting porous silicon carbide (SiC) to allow for coolant passage. The SiC had been ultrasonically machined to provide for larger coolant flow in certain areas and for posts to support the faceplate. The machining was done prior to a layer of silicon (Si) being deposited onto the outer surface of reaction sintered SiC. The Si deposition was done at a high temperature (above 1000°C).

UTOS reported the cracking of the SiC was noticed several days after a successful pressure test, using water, was performed on the cooled mirror assembly. A white crystalline-like material, Figures 23 and 24, formed within the porous structure which could not be readily explained.

In an effort to determine the chemistry of the white substance, scanning electron microscopy (SEM), x-ray diffraction (XRD) with an energy dispersive x-ray analyzer (EDAX), and Auger electron spectroscopy examinations were made on the materials involved. The SEM, EDAX, and XRD studies confirmed that the porous material was composed of Si and Ca with traces of Mg, Al, K, Mn, and Fe, but nothing more in the way of elements higher in atomic number than Na (atomic number 11) (Figures 25 and 26). The elements were assumed to be present in the SiC raw material or in the cooling water.



Figure 23. White crystalline-like "corrosion" material found in the area of the face-plate support posts (25X).

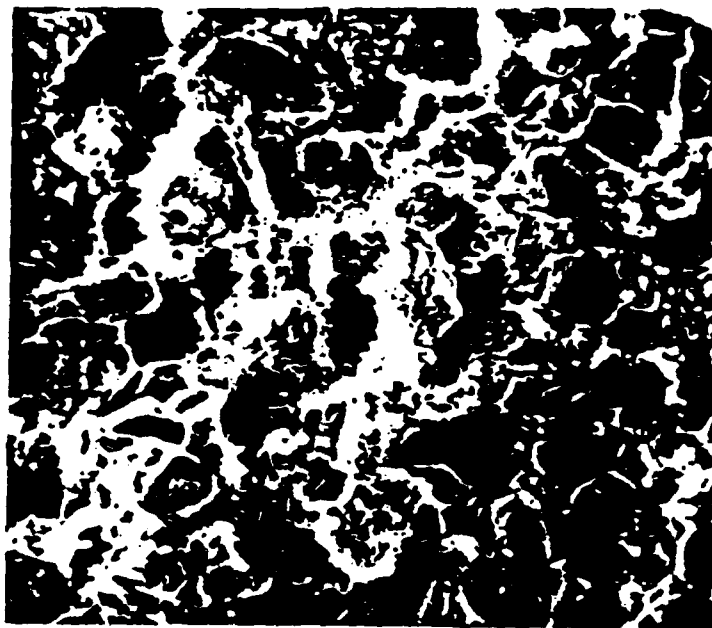


Figure 24. SEM photomicrograph of porous SiC with "corrosion" material filling the pores.

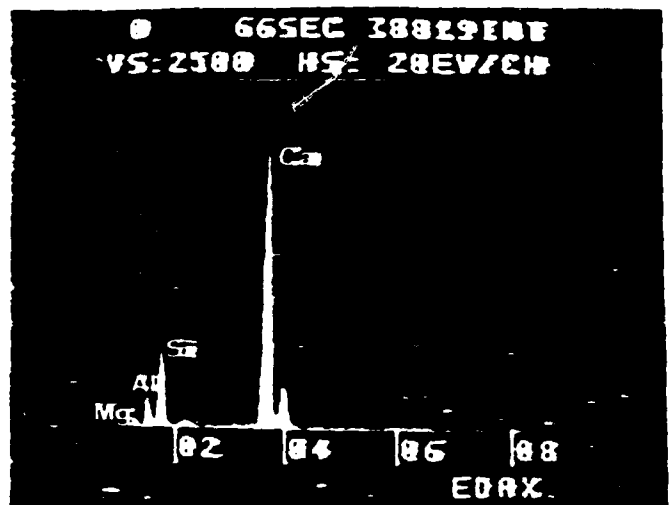


Figure 25. EDAX scan of porous SiC and contaminant showing the presence of Mn, Ca, Si, and Al.

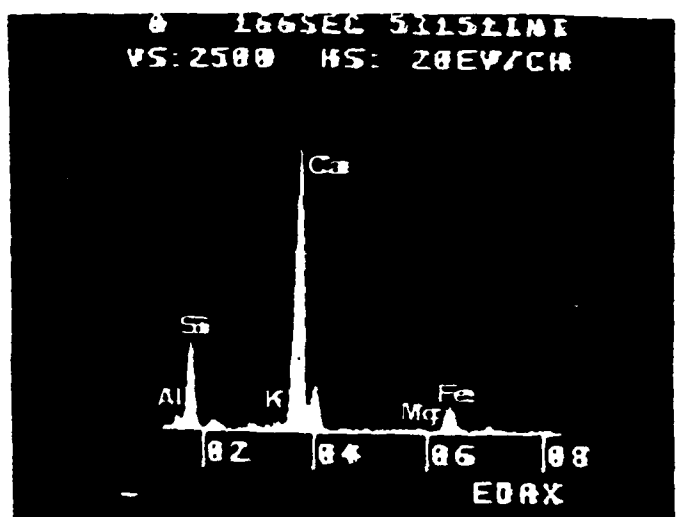


Figure 26. EDAX scan of porous SiC and contaminant showing the presence of Al, Si, K, Ca, Mg, and Fe.

The results of the XRD analysis shown in Table 2 confirmed that the bulk porous material was only SiC. The Auger analysis, however, is more sensitive to the lighter elements and indicated the presence of O and B. Figures 27, 28, and 29 are ACS scans taken confirming that the contaminant was B and also a small amount of Fe. At the time, the presence of boron was not understood until it was discovered that boron carbide (B_4C) was used as the cutting agent in the ultrasonic machining operation. Figure 30 shows two regions investigated. Region 1 was a fracture area of a machined SiC post and region 2 an area of white "deposite". Figures 31 and 32 are magnified areas of regions 1 and 2, respectively.

Further studies using an electron spectroscopy for chemical analysis apparatus (ESCA) (Figure 33) confirmed the Auger analysis and led to the conclusion that a borosilicate was formed through the combination of Si, B, O, and high temperature. The binding energy of the boron 1s peak, 192.7 eV, is quite close to that reported for B_2O_3 (193.0 eV). From the XPS data, there was no evidence of B_4C which should have a boron 1s peak at 186 eV. The silicon 2p peak is rather broad and asymmetrical. This is probably due to the presence of both SiC (peak at 100 eV) and an Si-O phase (peak at 102-103 eV). The oxygen 1s peak is also rather broad; this may be due to the fact that both hydroxides and oxides are present.

From the combination of data and optical observations it is now assumed that the glass formed is hydroscopic; in the presence of moisture it hydrolyzes, forming the white substance within the porous SiC and attacks the SiC in a corrosive manner causing cracking. These assumptions have not been conclusively confirmed. If required, future work would be directed to providing substantiating evidence.

TABLE 2
COOLED MIRROR POROUS SiC SURFACE

SiC(12H)

<u>2θ</u>	<u>D-Spacing</u>	<u>Intensity</u>
28.2	3.164	2
28.65	3.116	2
34.25	2.618	40
35.0	2.564	4
35.75	2.512	100
37.7	2.386	6
38.3	2.35	40
38.9	2.315	2
41.55	2.173	12
45.45	1.996	3
47.55	1.912	1
54.75	1.677	8
56.35	1.633	4
60.1	1.539	42
65.75	1.42	12
67.0	1.397	2
71.0	1.328	4
71.85	1.314	27
73.45	1.289	3
73.7	1.285	2

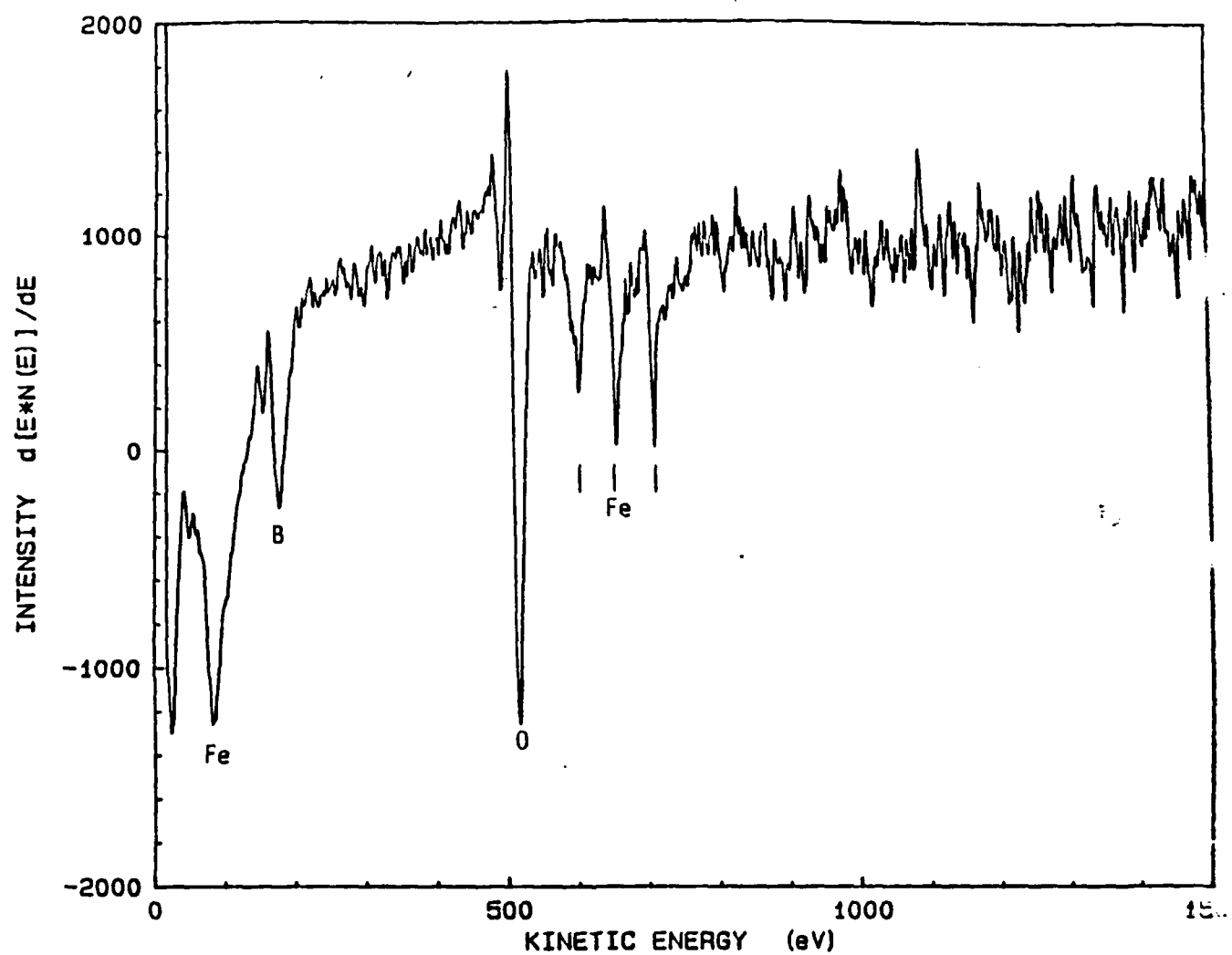


Figure 27. Laser mirror mount contaminated region 1.

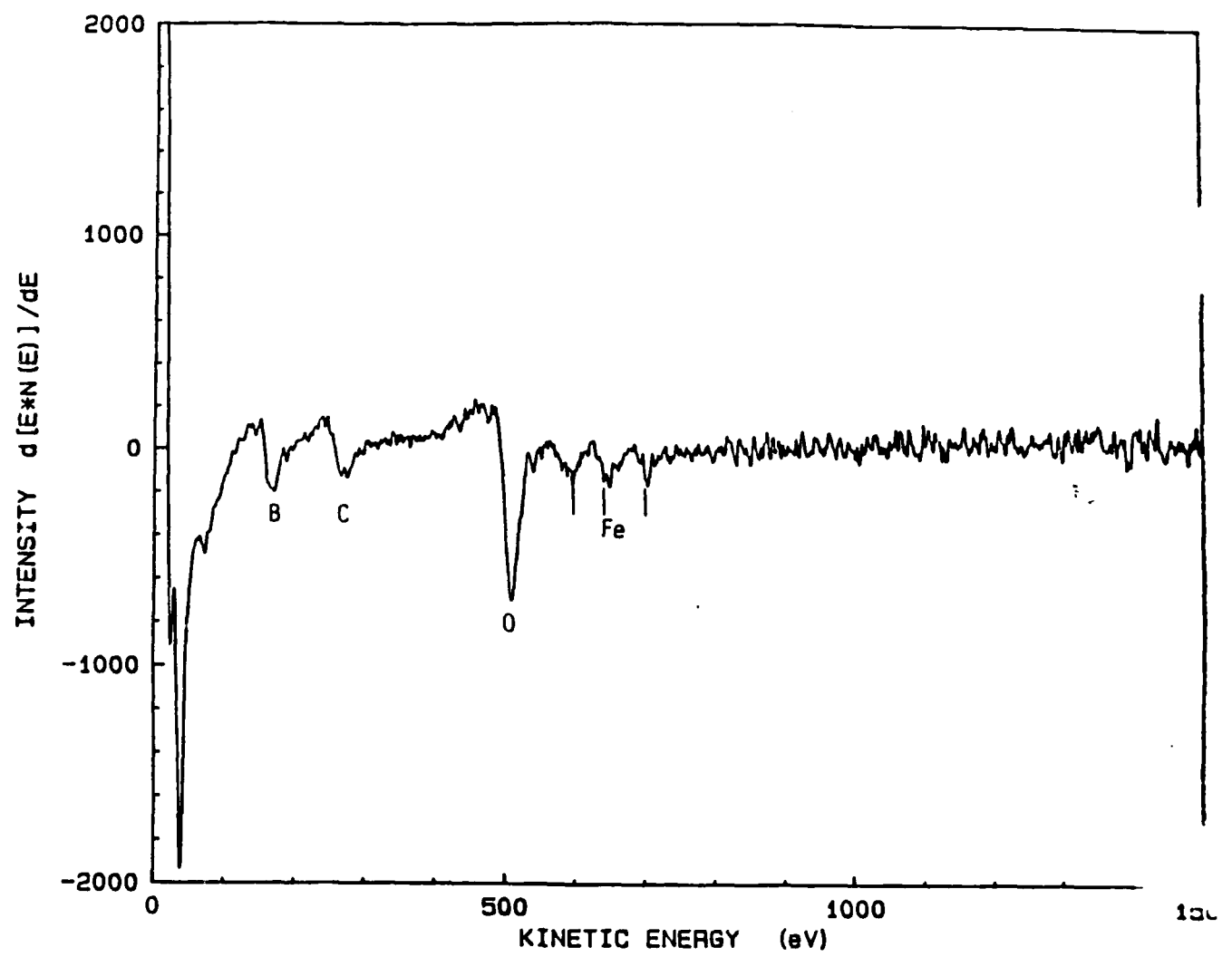


Figure 27. Laser mirror mount contaminated region 1 (continued).

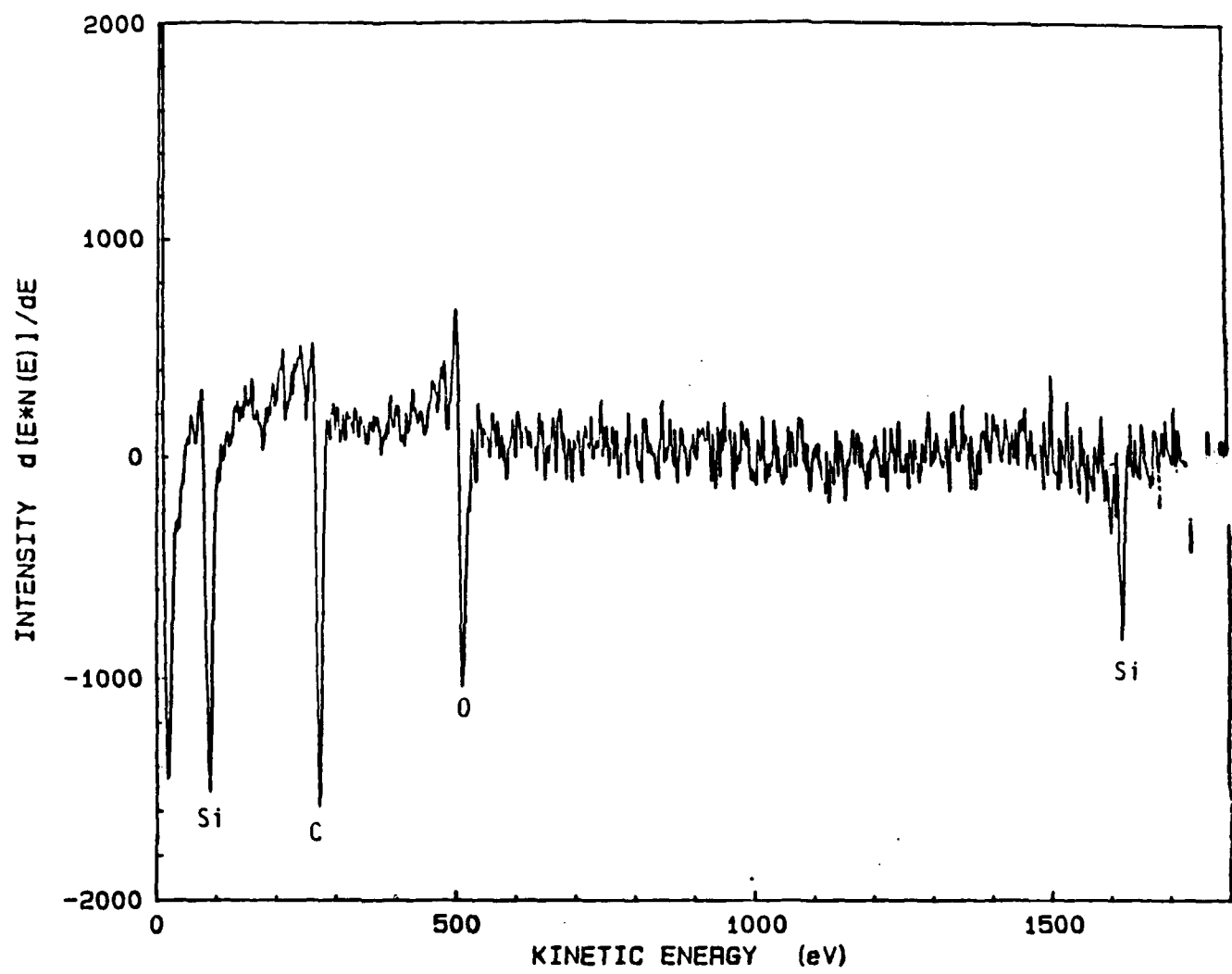


Figure 27. Laser mirror mount contaminated region 1 (concluded).

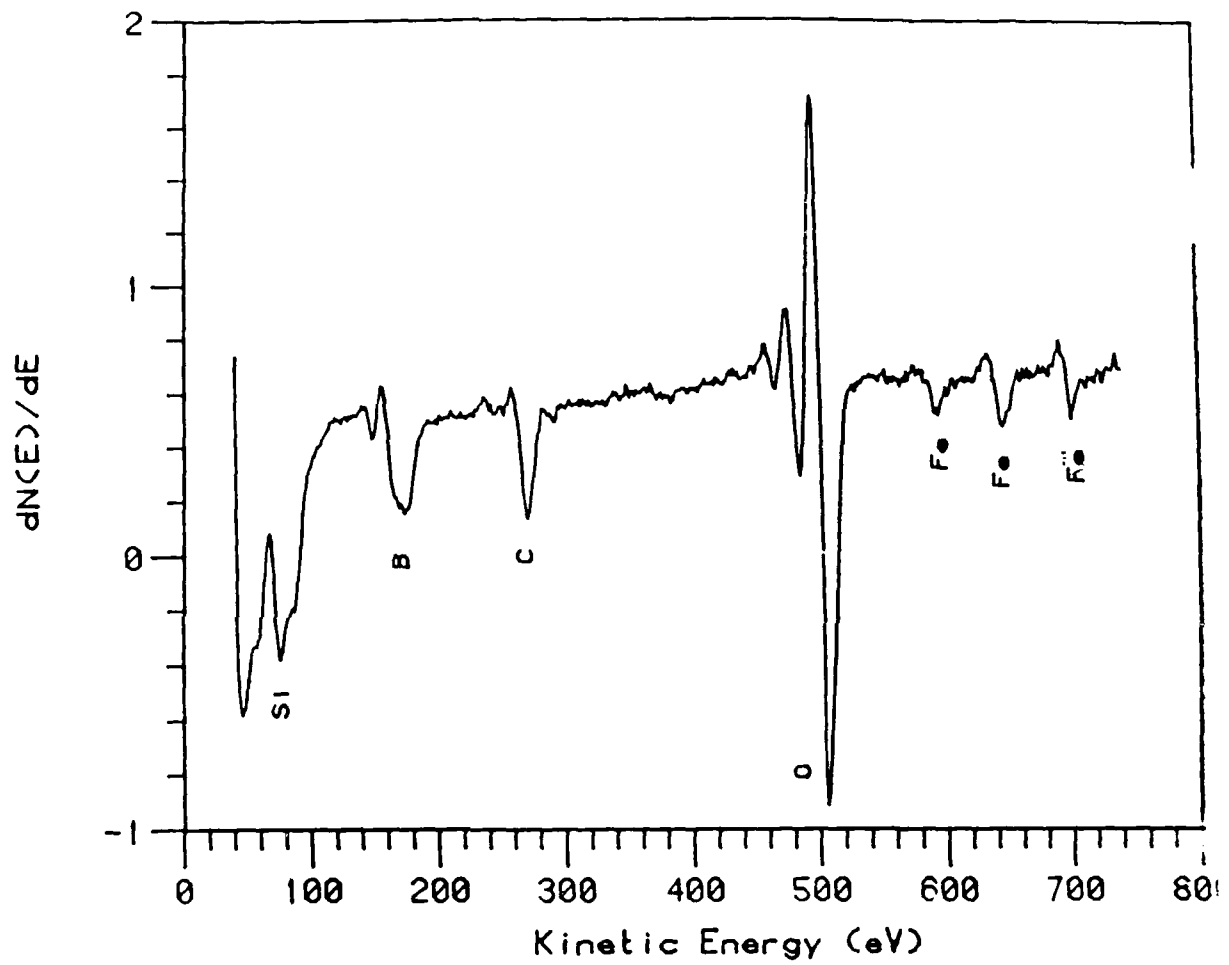


Figure 28. SiC piece next to region with pin broken off AES scan.

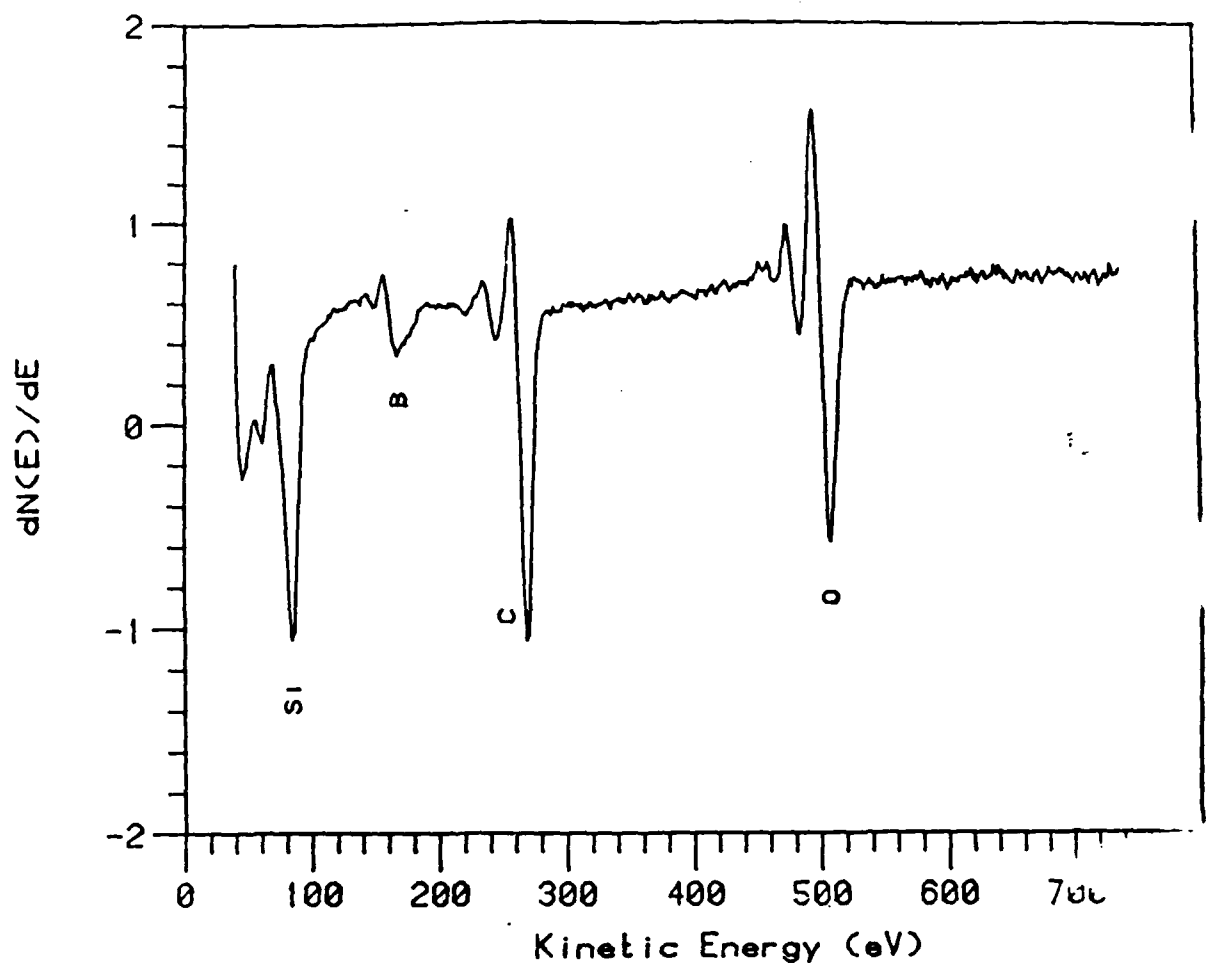


Figure 28. SiC piece next to region with pin broken off AES scan (continued).

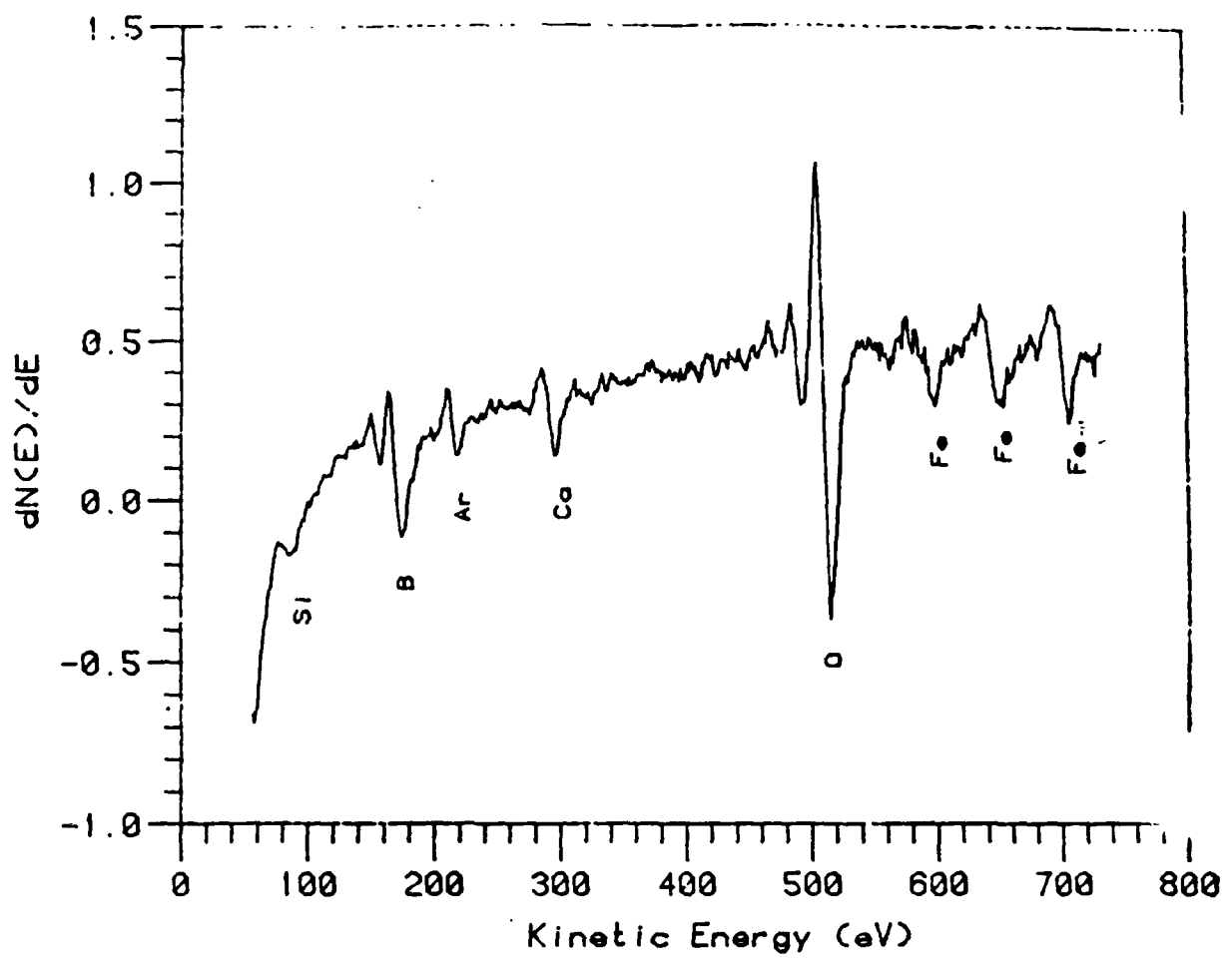


Figure 28. SiC piece next to region with pin broken off AES scan (continued).

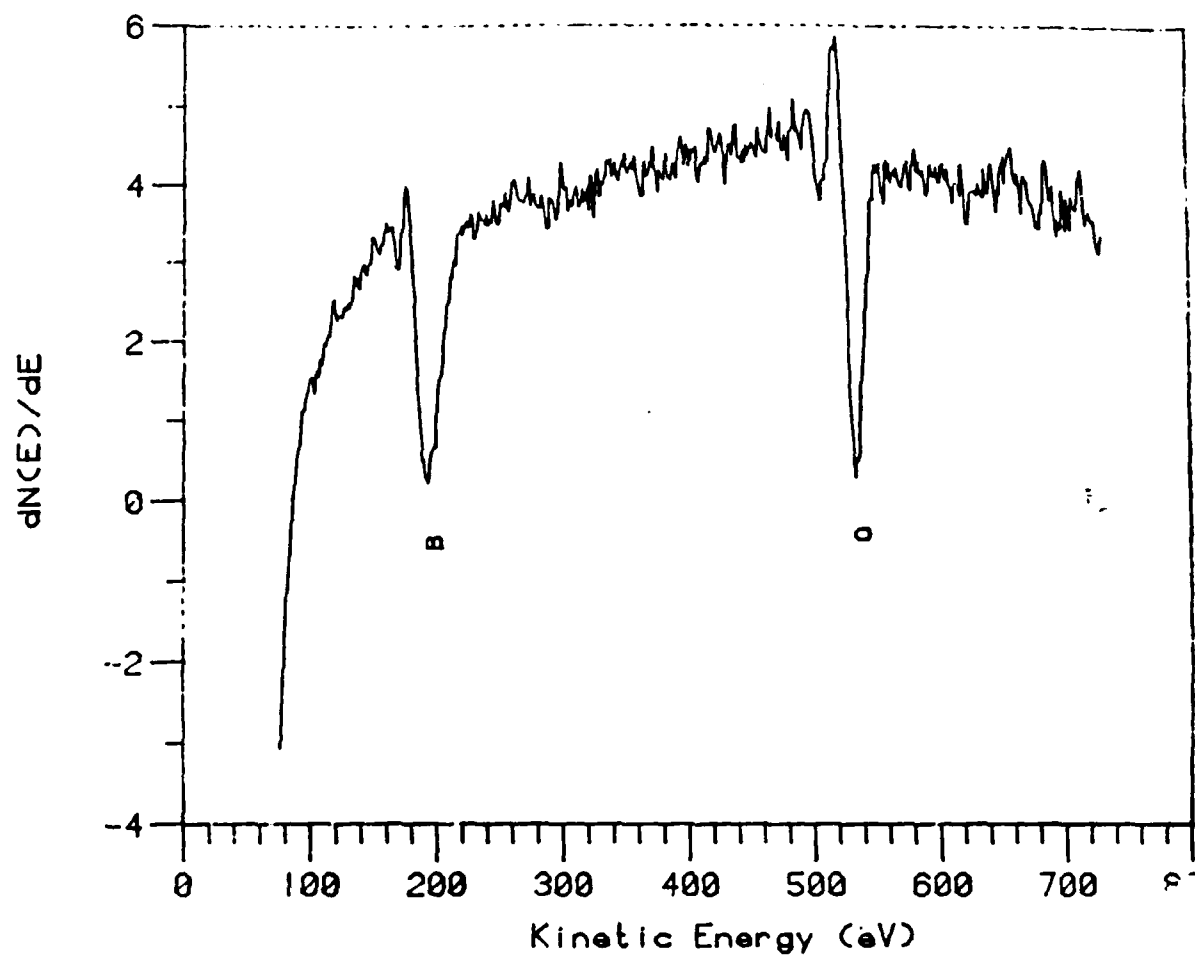


Figure 28. SiC piece next to region with pin broken off AES scan (continued).

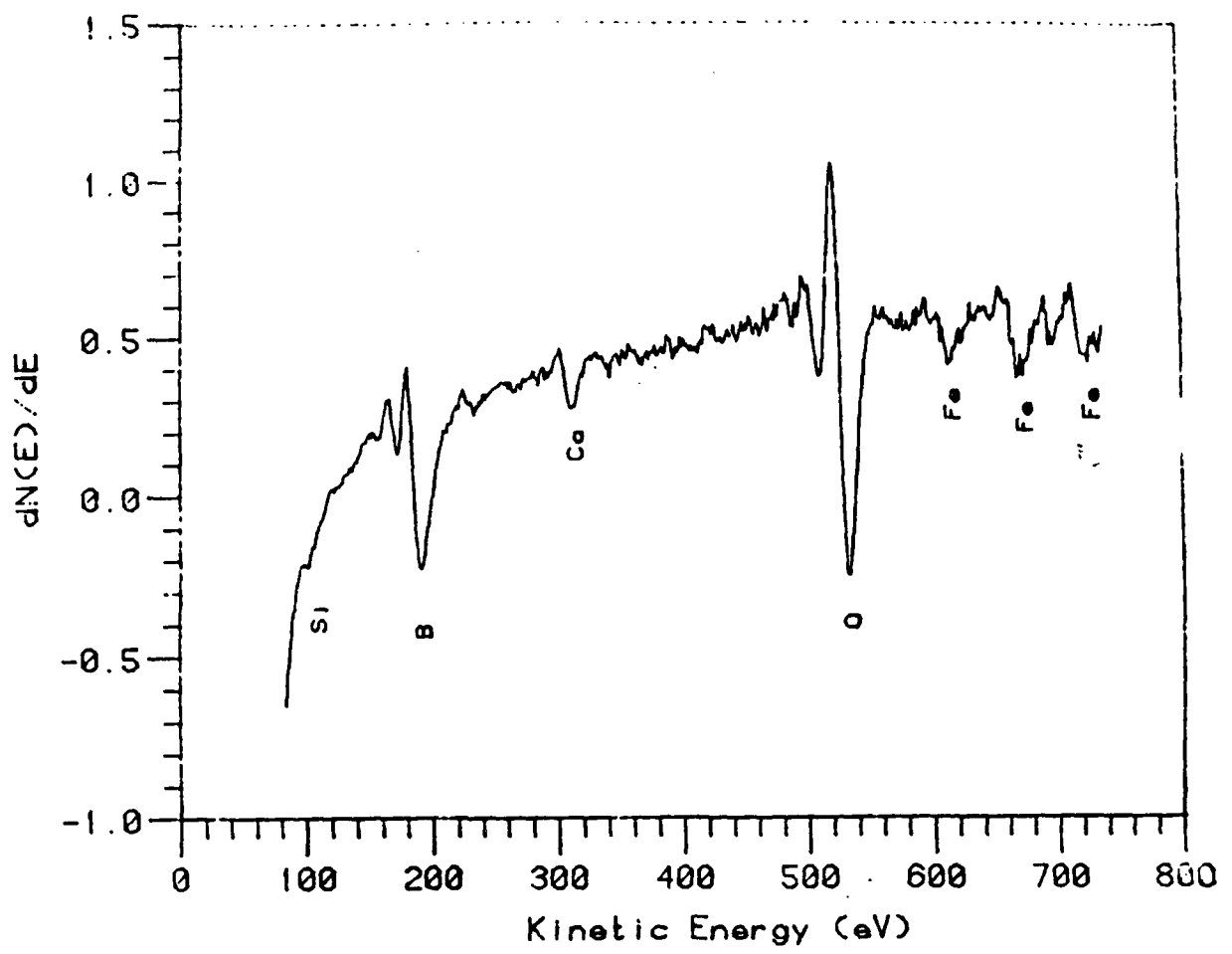


Figure 28. SiC piece next to region with pin broken off AES scan (continued).

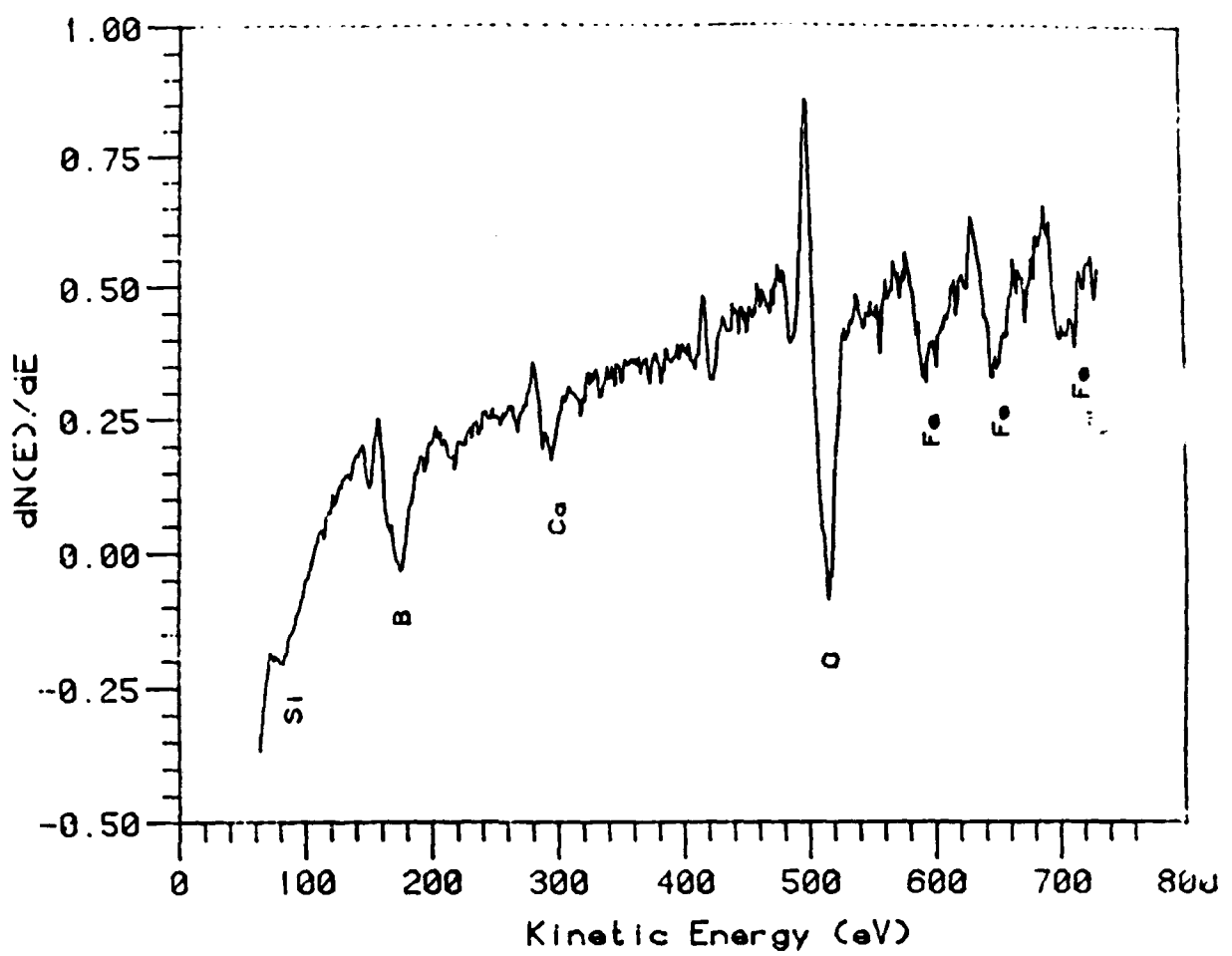


Figure 28. SiC piece next to region with pin broken off AES scan (concluded).

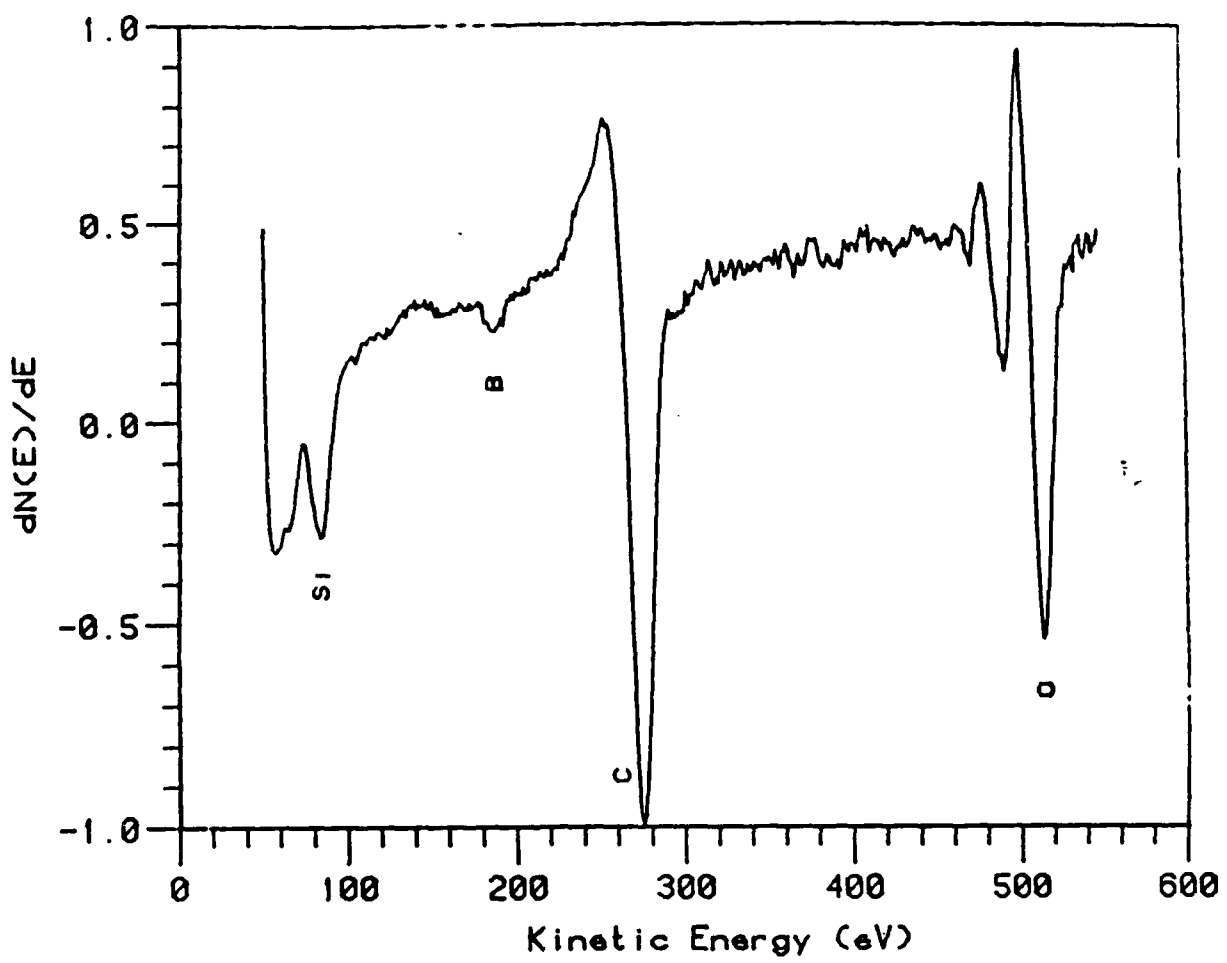


Figure 29. SiC and B_4C AES surface scan.

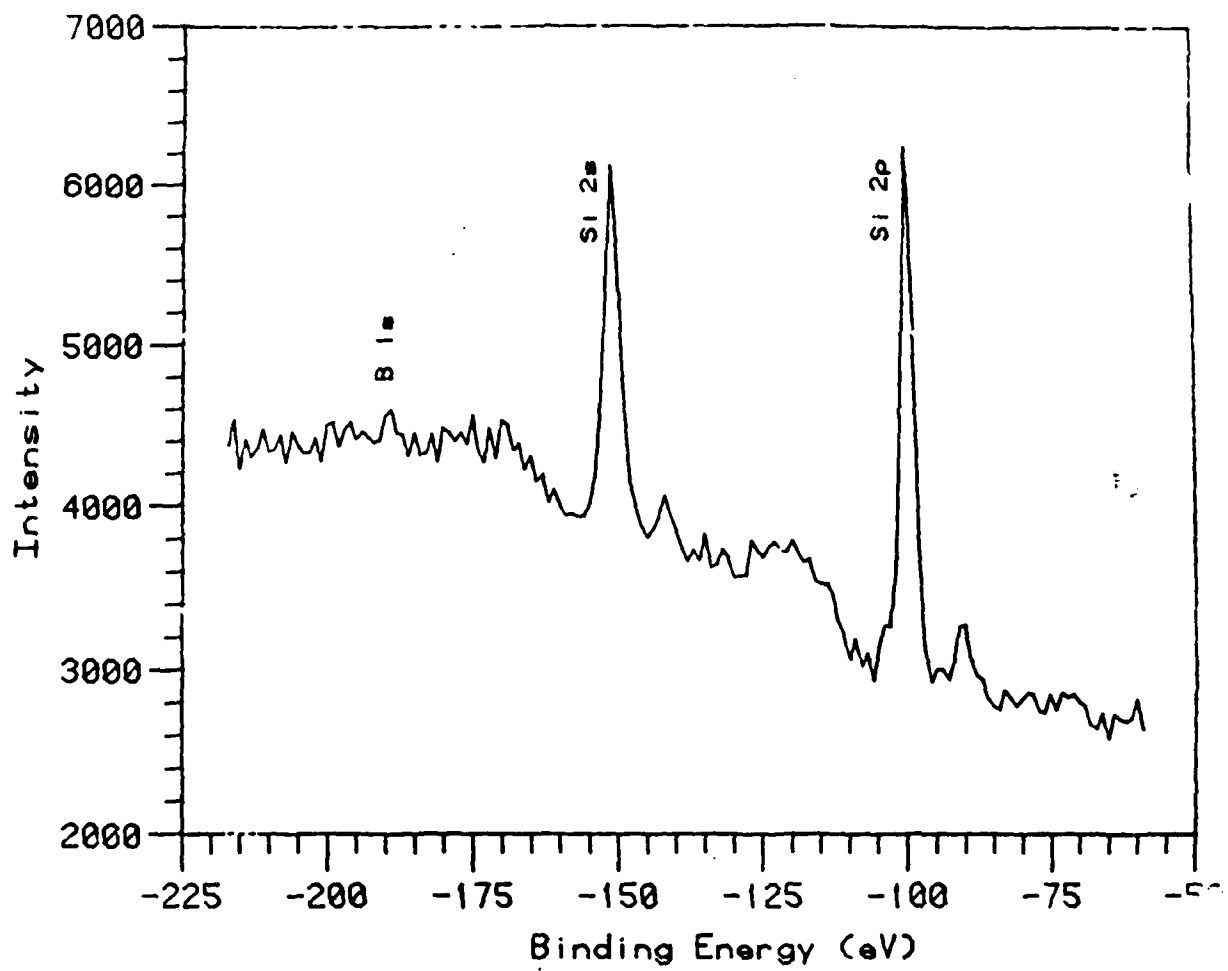


Figure 29. SiC and B_4C AES surface scan (continued).

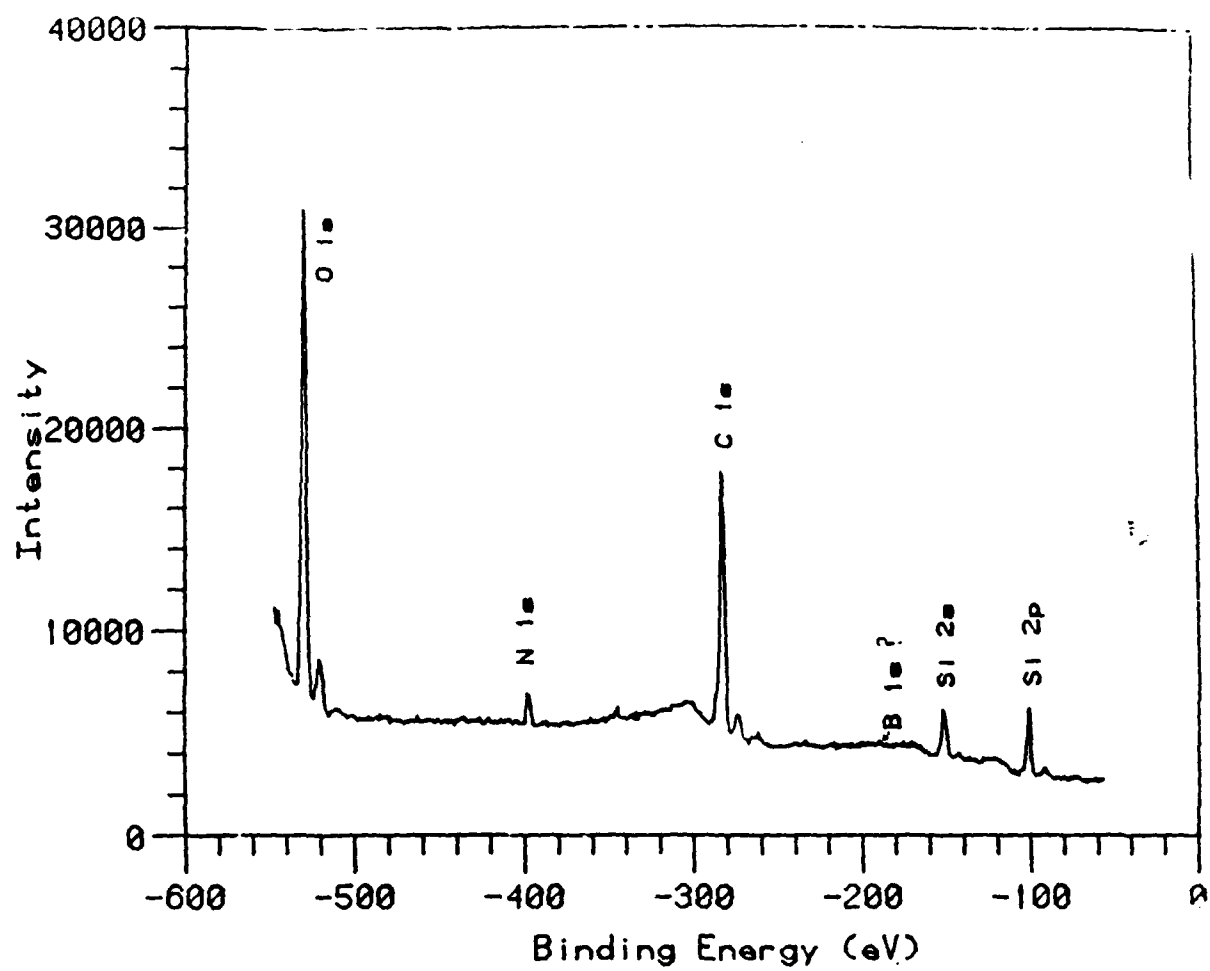


Figure 29. SiC and B_4C AES surface scan (concluded).



Figure 30. SEM photomicrograph of fracture porous SiC (region 1) and contaminant (region ?) as observed by ACS.

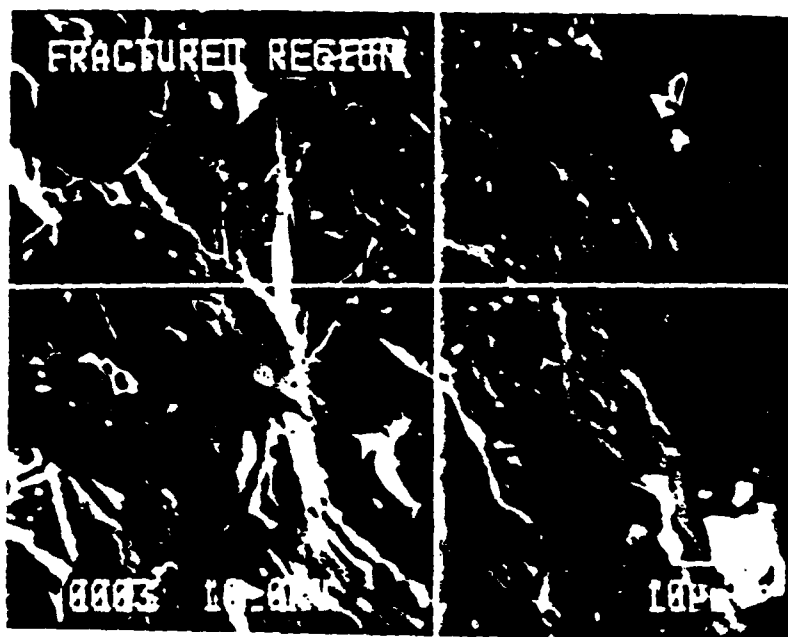


Figure 31. SEM photomicrograph of region 1.

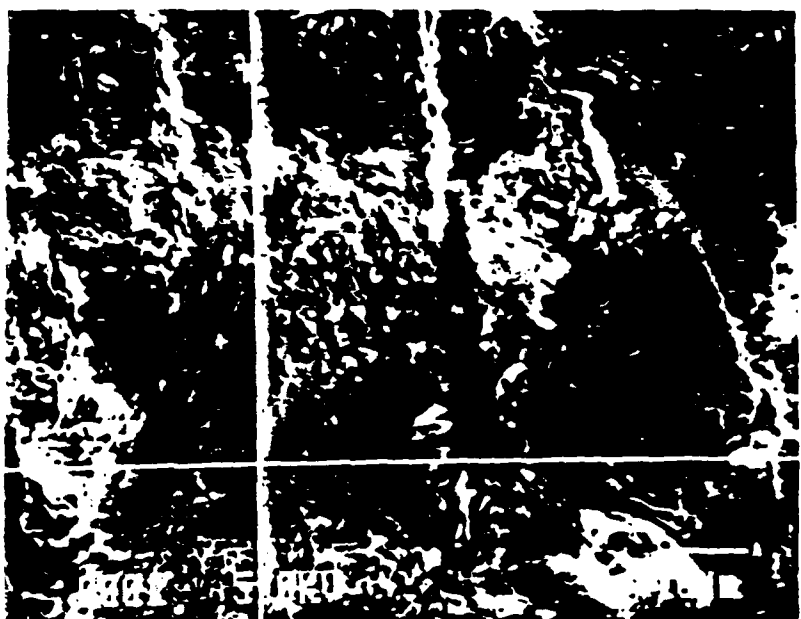


Figure 32. SEM photomicrograph of region 2.

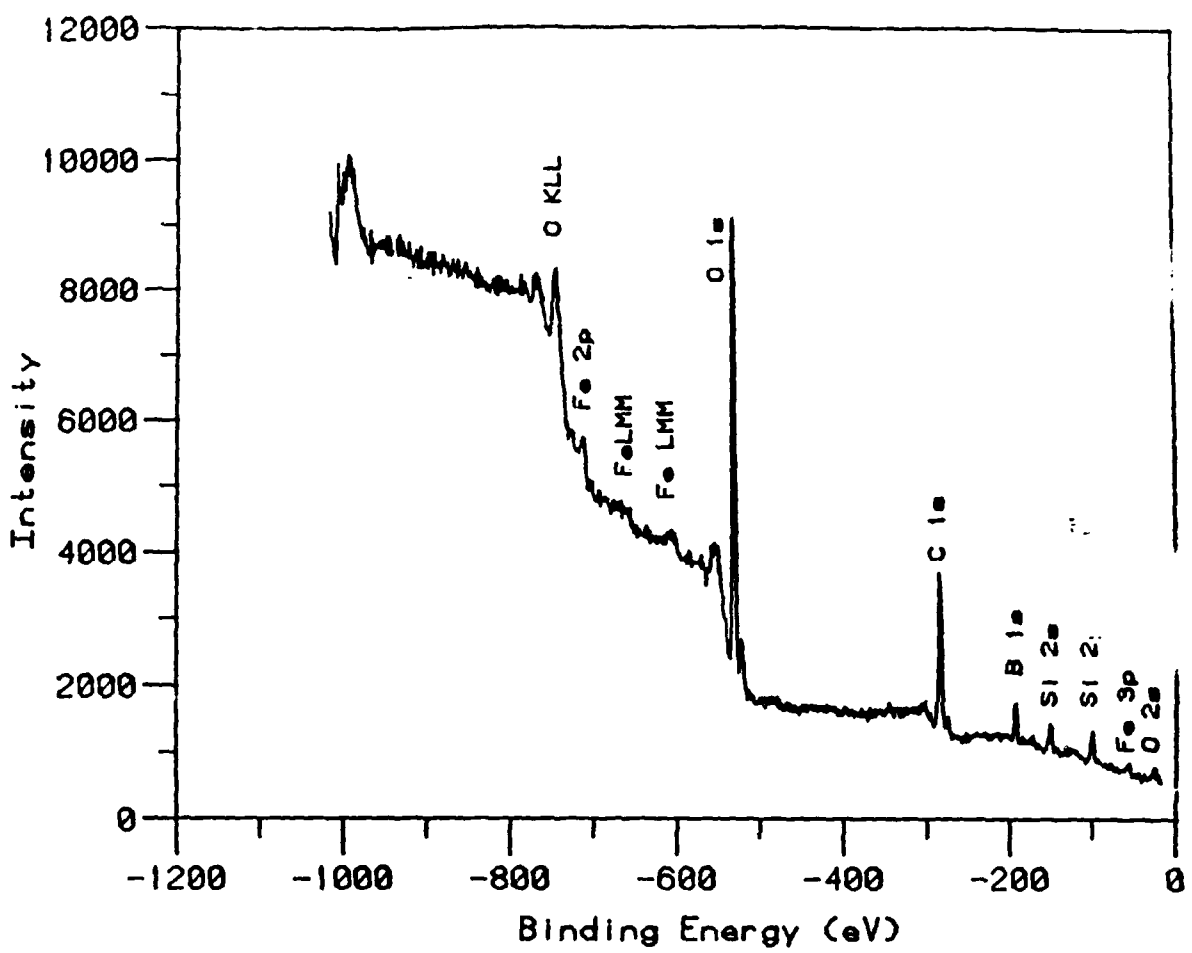


Figure 33. Porous SiC (side w/pins broken off) ESCA surface scan.

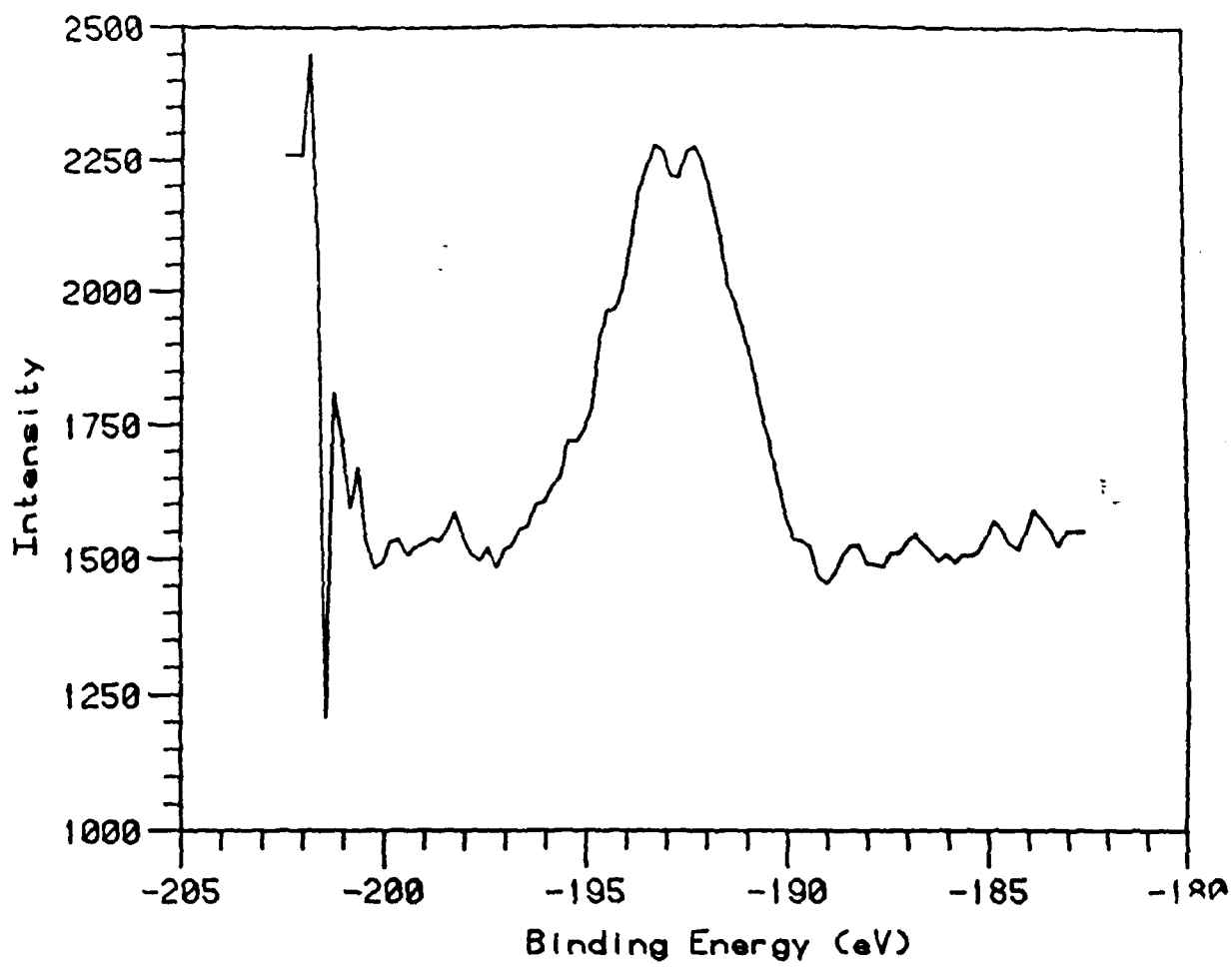


Figure 33. Porous SiC (side w/pins broken off) ESCA surface scan (continued).

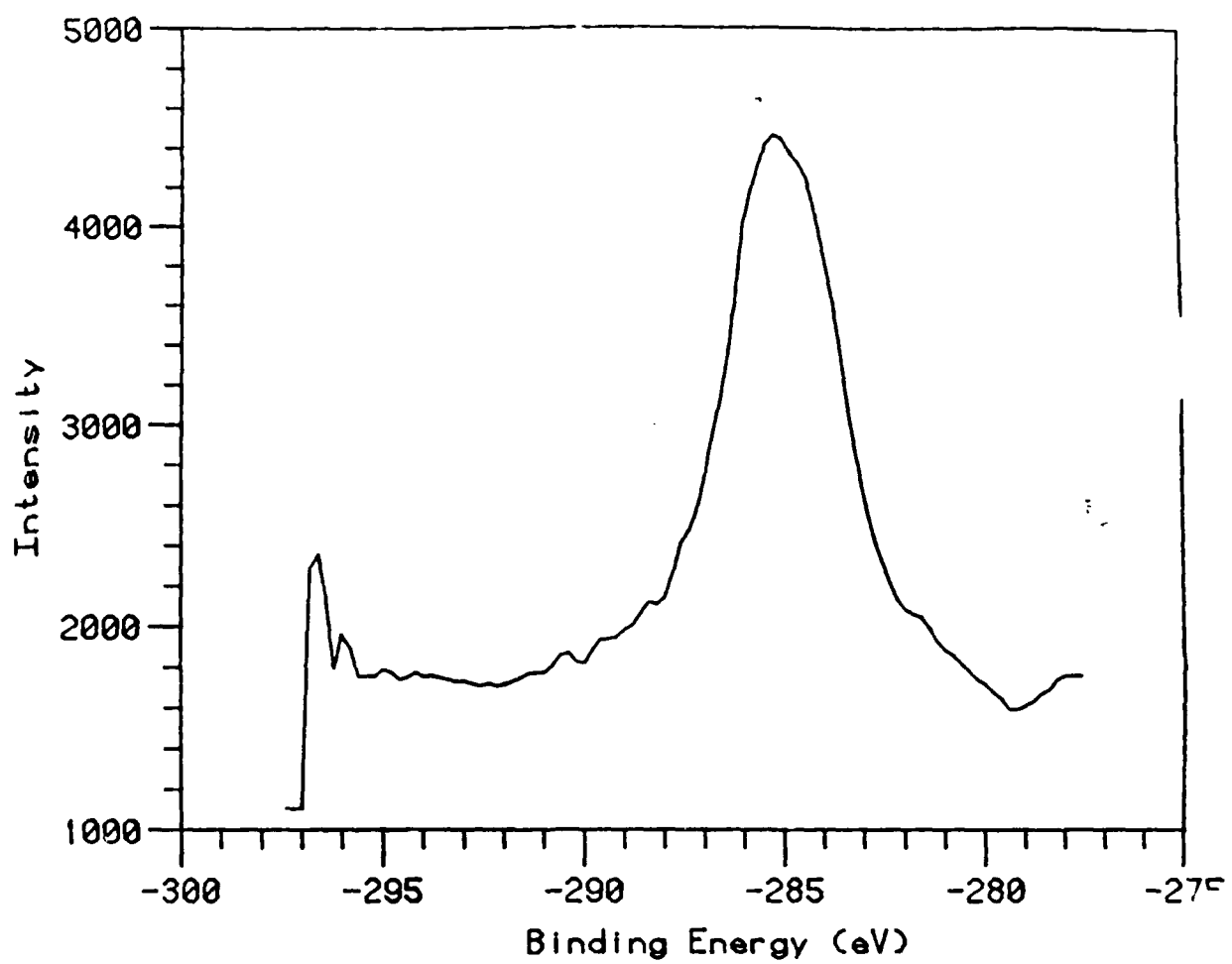


Figure 33. Porous SiC (side w/pins broken off) ESCA surface scan (continued).

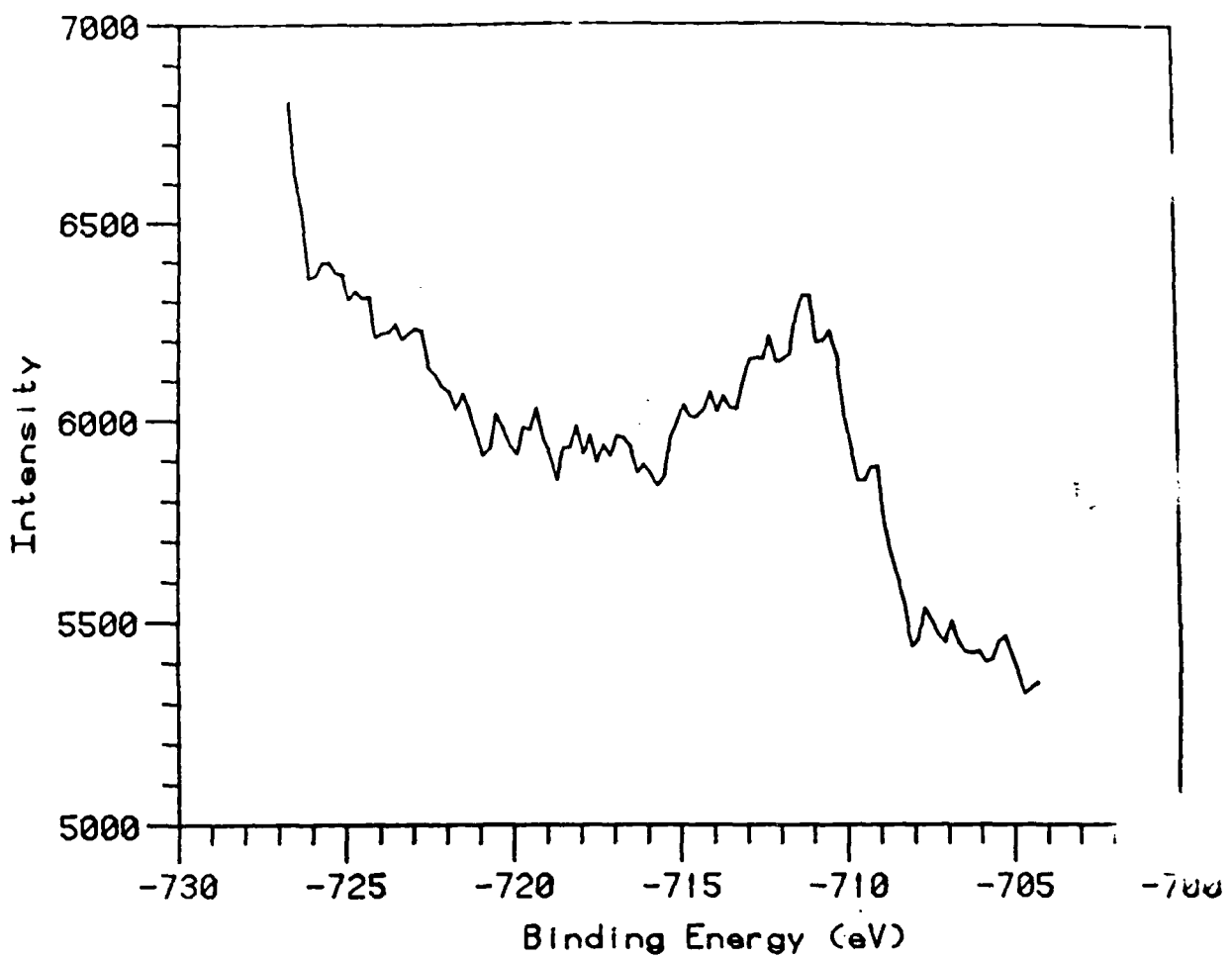


Figure 33. Porous SiC (side w/pins broken off) ESCA surface scan (continued).

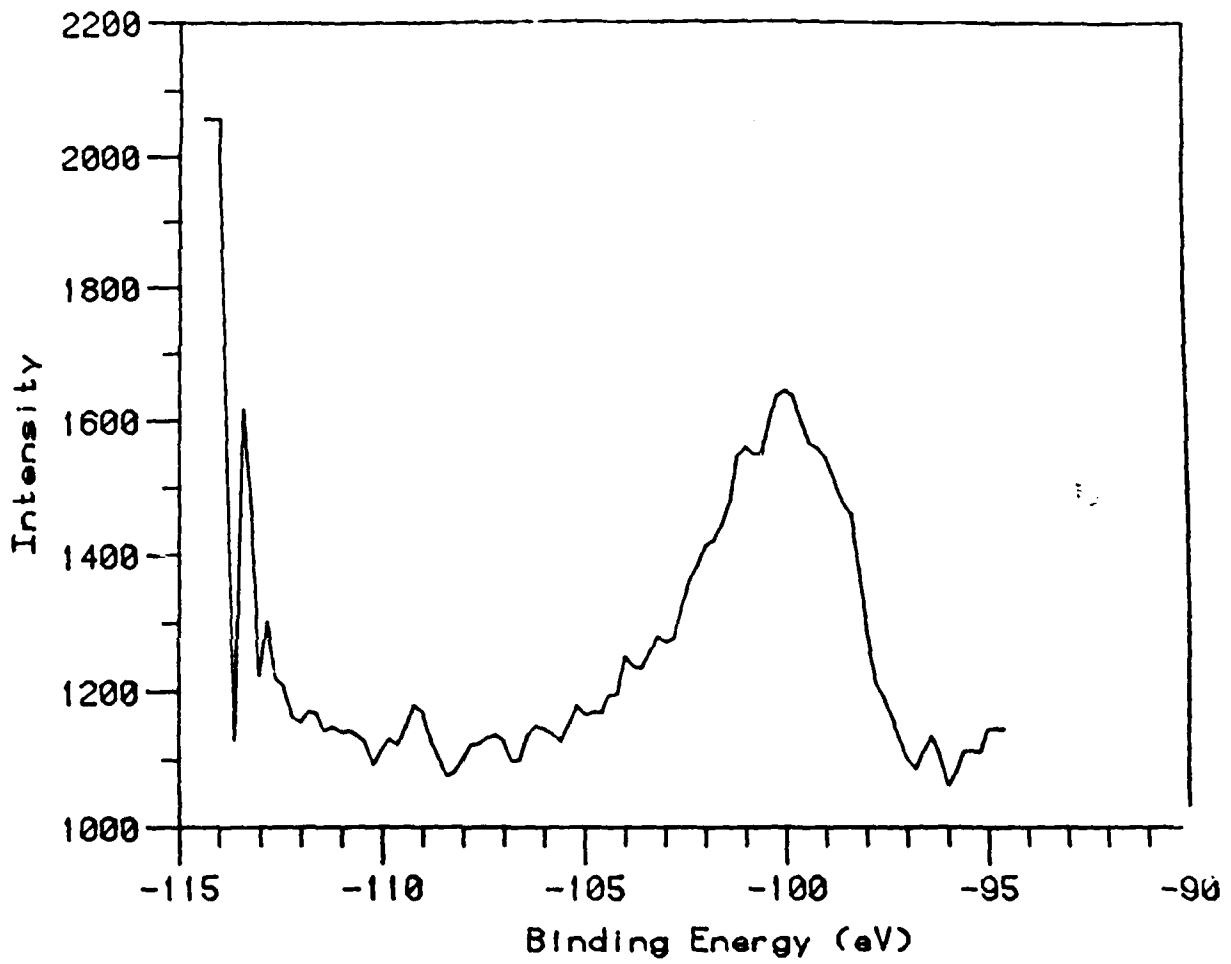


Figure 33. Porous SiC (side w/pins broken off) ESCA surface scan (continued).

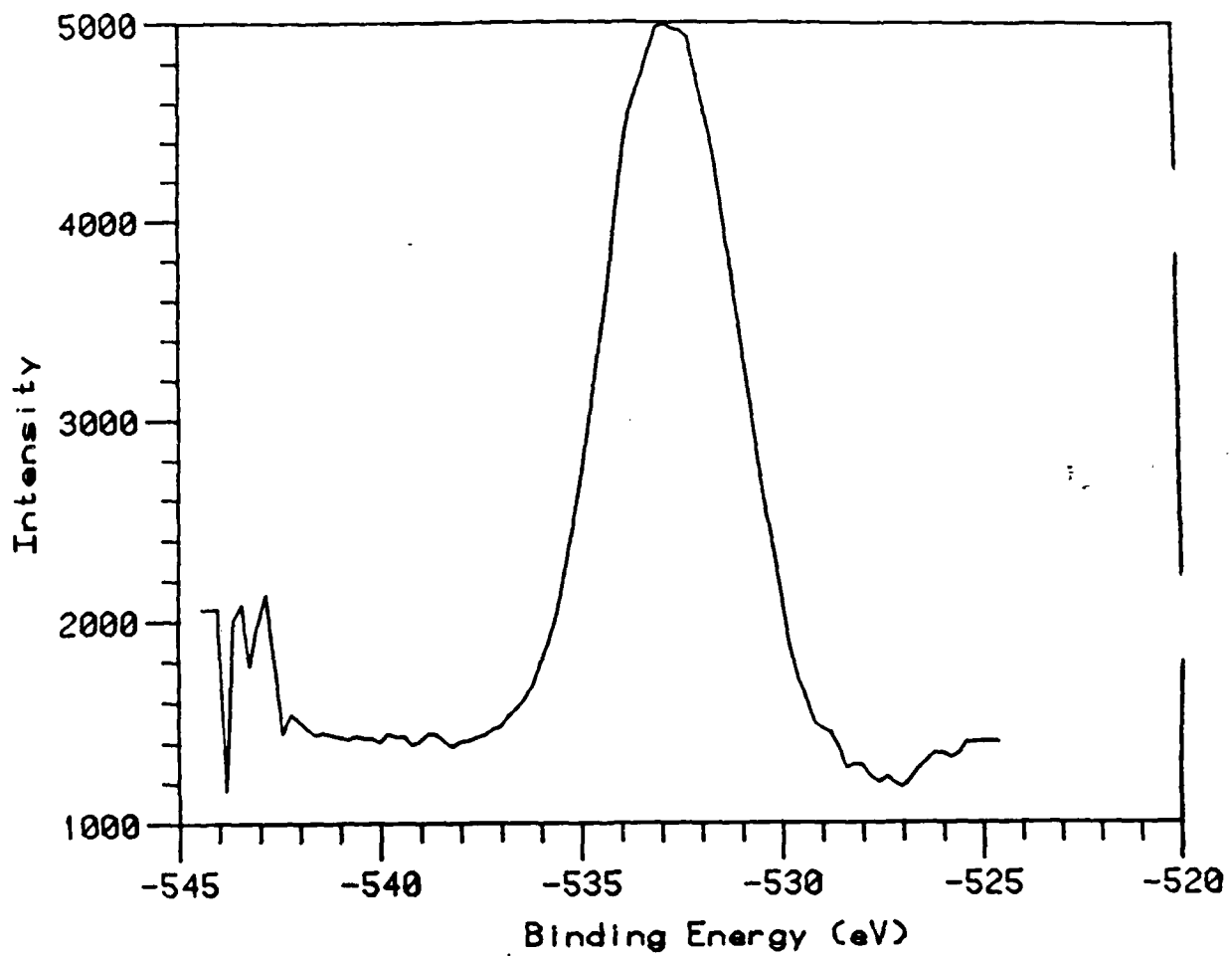


Figure 33. Porous SiC (side w/pins broken off) ESCA surface scan (concluded).

APPENDIX A

Material Type: CVD Si (Polycrystalline)

Manufacturer: CVD Incorporated

Test Temperature: 25°C

Number of Specimens: 5

Specimen Size: 0.33 x 0.25 x 7.6 cm

4-Pt. Bend Strength: 221 MPa (32 ksi)

Standard Deviation: 33 MPa (4.8 ksi)

Young's Modulus:

Poisson's Ratio: 0.25

Vickers Hardness (100 gm load): 772 (ave. of 3 specimens)

K_{IC} (ave. of 3 specimens): 0.9 (std. dev.: 0.06)

CTE (25°C to 1000°C): $\alpha = 3.6 \times 10^6 / ^\circ\text{C}$

Specific Heat (cal/gm°C):

<u>75°C</u>	<u>125°C</u>	<u>175°C</u>	<u>225°C</u>	<u>275°C</u>
0.18	0.20	0.18	0.20	0.21

Comments:

The microstructure for this material was found to be composed of a very fine dendritic structure with the long axis of the dendrites being oriented along the deposition direction. The dendrites appeared to be clustered in a rosette type formation. In addition to the bend strengths shown above, five specimens from the same processing run were chemically etched after polishing. The average 4-pt. bend strength for these specimens was 243 MPa (35.1 ksi). All of the CVD prepared specimens were diamond ground and polished to a metallographic finish. The surfaces of all the specimens contained a small number of residual grinding marks. The edges of each specimen were rounded. Nearly all of the edges contained small chips and all of them contained grinding marks. The majority of the fracture initiation sites were found in tensile surface. There was no correlation between low strength and edge failure, and all fracture strengths were included to obtain the average fracture strength.

Material Type: CVD Si (Polycrystalline)

Manufacturer: Raytheon Corporation

Test Temperature: 25°C

Number of Specimens: 5

Specimen Size: 0.56 x 0.33 x 6.4 cm

4-Pt. Bend Strength: 159 MPa (23.1 ksi)

Standard Deviation: 28 MPa (4.1 ksi)

Thermal Diffusivity at Room Temp.: 0.62 $\text{cm}^2 \text{s}^{-1}$

Specific Heat (cal/gm°C):

<u>75°C</u>	<u>125°C</u>	<u>175°C</u>	<u>225°C</u>	<u>275°C</u>
0.18	0.19	0.19	0.20	0.20

Comments:

The microstructure for this material was found to be composed of a very fine dendritic structure with the long axis of the dendrites being oriented along the deposition direction. The dendrites appeared to be clustered in a rosette type formation. All of the CVD prepared specimens were diamond ground and polished to a metallographic finish. The surfaces of all the specimens contained a small number of residual grinding marks. The edges of each specimen were rounded. Nearly all of the edges contained small chips and all of them contained grinding marks. The majority of the fracture initiation sites were found in tensile surface. There was no correlation between low strength and edge failure, and all fracture strengths were included to obtain the average fracture strength.

Material Type: CVD SiC (3-polycrystalline)

Manufacturer: CVD Incorporated

Test Temperature: 25°C

Number of Specimens: 4

Specimen Size: 0.33 x 0.25 x 7.6 cm

4-Pt. Bend Strength: 554 MPa (80 ksi)

Standard Deviation: 119 MPa (17.4 ksi)

Young's Modulus: 475 GPa (69×10^{-6} psi)

Vickers Hardness (500 gm load): 2600

K_{IC} (ave. 3 specimens): 2.6 N/m^{3/2}

CTE (25°C to 500°C): $4.1 \times 10^{-6}/^{\circ}\text{C}$

Specific Heat (cal/gm°C):

<u>75°C</u>	<u>125°C</u>	<u>175°C</u>	<u>225°C</u>	<u>275°C</u>
0.19	0.21	0.23	0.25	0.26

Comments:

The test specimens in this group were all prepared by cutting the material to shape on a diamond cut-off wheel and finishing the surfaces by diamond grinding and polishing. All of the surfaces of interest were prepared with a metallographic finish, however, minor scratches were observed on all surfaces at 30X using white light.

When etched, a dendritic type microstructure was observed with the long axis of the grains in the deposition direction. The grain diameter was in the 0-1 μm to 2 μm range perpendicular to the growth direction with a higher percentage of small grains at the mandrel surface.

Material Type: CVD SiC (β -polycrystalline)

Manufacturer: Raytheon Corporation

Test Temperature: 25°C

Number of Specimens: 7

Specimen Size: 0.33 x 0.25 x 7.6 cm

4-Pt. Bend Strength: 422 MPa (61 ksi)

Standard Deviation: 151 MPa (22 ksi)

Vickers Hardness (500 gm load): 2534 (std. dev.: 142)

K_{IC} (ave. 8 specimens): 5.3 ($N/m^{3/2}$) (std. dev.: 0.4)

Comments:

All this material was prepared in a nearly identical procedure as the Group 1 CVD Si. There is evidence that the processing parameters may have changed during the processing run. This showed up in an examination of the fracture surfaces of the flexural strength specimens where a "layering" effect was observed. This may have caused a residual stress, and/or microcracking that led to a lower average strength and increased scatter in the data.

Material Type: Single Crystal Silicon

Group 1

Test Temperature: 25°C
Number of Specimens: 14
Specimen Size: 5.7 x 1.0 x 0.6 cm
4-Pt. Bend Strength: 137 MPa (20 ksi)
Standard Deviation: 32.6 MPa (4.7 ksi)
Young's Modulus: 170 GPa (25×10^6 psi)
Poisson's Ratio: 0.26
Knoop Hardness: 195 (ave. of 10 specimens)

Test Temperature: 290°C
Number of Specimens: 14
4-Pt. Bend Strength: 132 MPa (19 ksi)
Standard Deviation: 46.9 MPa (6.7 ksi)

Comments:

Material was diamond ground - final grind with 600 grit diamond, then chemically etched. Mechanical test specimens had beveled edges, and many surface scratches were observed at 30X. Flexure strength specimens were randomly oriented. The Young's modulus specimens were prepared with the strain gages on (111) surfaces. Many specimens failed at the edges, but no correlation was found between strength and fracture initiation site.

Material Type:

Single Crystal Silicon

Group 2

Test Temperature: 25°C
Number of Specimens: 24
Specimen Size: 5.7 x 0.9 x 0.6 cm
4-Pt. Bend Strength: 116 MPa (17 ksi)
Standard Deviation: 31.4 MPa (4.5 ksi)
Young's Modulus: 191 GPa (28×10^6 psi)
Poisson's Ratio: 0.20

Test Temperature: 290°C
Number of Specimens: 23
Specimen Size: 5.7 x 0.9 x 0.6 cm
4-Pt. Bend Strength: 142 MPa (21 ksi)
Standard Deviation: 34.9 MPa (5.1 ksi)

Thermal Expansion:

<u>Temp. Range (°C)</u>	<u>CTE ($\times 10^{-6} \text{°C}^{-1}$)</u>
40-50	2.5
90-100	2.3
140-150	2.6
190-200	3.0
240-250	3.1
275-285	2.9

Comments:

The test specimens were prepared using two different grinding techniques (undefined) and then chemically etched. Edges were beveled. The final surface's appearance when viewed at 30X were covered with longitudinal and transverse scratches. The chemical etch appeared to be severe. Approximately half of the specimens failed at the beveled edges, however no correlation between failure initiation site and strength was found. The higher strength at 290°C may have been the result of flaw healing. The Young's modulus values were determined with the strain gages on (111) surfaces.

Material Type: Single Crystal Silicon

Group 3

Test Temperature: 25°C
Number of Specimens: 25
Specimen Size: 5.7 x 1.0 x 0.6 cm
4-Pt. Bend Strength: 116 MPa (17 ksi)
Standard Deviation: 31 MPa (4 ksi)

Test Temperature: 290°C
Number of Specimens: 23
Specimen Size: 5.7 x 1.0 x 0.6 cm
4-Pt. Bend Strength: 142 MPa (21 ksi)
Standard Deviation: 35 MPa (5 ksi)

Comments:

The surfaces of all the specimens were scratched; some in the longitudinal direction and some with multi-direction (longitudinal, transverse and/or random). The direction of the surface grinding was still detectable although the specimens had been etched. The majority of the specimens appeared to have been ground diagonally, but some of the group displayed diagonal grinding marks on one face with longitudinal grinding marks on the opposite face. The edges were beveled and contained small chips.

Material Type:

SiC-poly-crystalline

Type: KT and SA

Characterization tests were performed on two commercially available silicon carbide materials received from Dr. A. Hopkins. The two materials were designated SA and KT. No further information was provided. The coefficient of thermal expansion was determined to be $2.5 \times 10^{-6}/^{\circ}\text{C}$ and $2.6 \times 10^{-6}/^{\circ}\text{C}$ for the type "SA" and type "KT" materials, respectively. The mean value for the ultimate strength of type "SA" material was 244.5 MPa (35.5 ksi) with standard deviation of 55.0 MPa (8.0 ksi) for the 4 sample group. The mean value for the ultimate strength of type "KT" material was 163.3 MPa (23.7 ksi) with standard deviation of 12.4 MPa (1.8 ksi) for this 5 sample group.

The fracture surfaces of the two types of material were observed to be distinctly different during post-test low power inspection. Both samples showed evidence of intergranular failure while the type "KT" sample also showed some transgranular failure indicated by the cleavage surfaces. Due to the mixed mode failure in the type "KT" material and the difference in ultimate strength of the two types of material, a compositional difference was suspected. Polished sections of both materials were prepared for EDXA examination. Both materials displayed porosity. The type "KT" material shows a definite compositional variation from the type "SA" material, but EDXA indicated only silicon to be present. A sample of each material was analyzed by x-ray diffraction. This analysis showed that the type "SA" material contained silicon carbide and that the type "KT" material contained a mixture of silicon carbide with a small amount of silicon.

Specific heat, thermal diffusivity, and bulk density were determined for both types of material. Thermal conductivity was calculated from the relationship:

$$k = C_p \alpha \rho$$

where:

k = thermal conductivity

C_p = specific heat

α = thermal diffusivity

ρ = bulk density

Table 1 contains the measured values of specific heat, thermal diffusivity and bulk density, and the calculated thermal conductivity corresponding to the temperature of parameter measurement. Bulk density was determined at room temperature only and is assumed to be relatively constant over the temperature range used for the calculation of thermal conductivity.

TABLE 1
Thermal Properties for Type "SA" and
Type "KT" Mirror Materials

Temperature (°C)	Type "SA"			
	C_p (cal/gm K)	α (cm ² /s)	ρ (gm/cm ³)	k (watt/cm°C)
25			3.15	
50	0.154	0.255		0.52
100	0.220	0.220		0.64
150	0.213	0.188		0.53
200	0.222	0.181		0.53
250	0.244	0.176		0.57
300	0.260	0.140		0.48
Type "KT"				
Temperature (°C)	C_p (cal/gm K)	α (cm ² /s)	ρ (gm/cm ³)	k (watt/cm°C)
25		3.07		
50	0.176	0.739		1.67
100	0.211	0.487		1.32
150	0.226	0.491		1.43
200	0.235	0.418		1.26
250	0.255	0.345		1.13
300	0.254	0.309		1.01